JGR Planets

RESEARCH ARTICLE

10.1029/2024JE008885

Northwest Africa 16788: The Largest Known Individual Martian Meteorite—A New Olivine Microgabbroic Shergottite and Its Implications for Martian Magmatism

Xhonatan Shehaj[1,2,3], Giovanni Pratesi[3,4], Cristian Carli[5], Riccardo Avanzinelli[3], Alice Stephant[3,6], Annarita Franza[1,3], and Eleonora Ammannito[2]

[1]Dipartimento di Fisica, Università degli Studi di Trento, Trento, Italy, [2]Agenzia Spaziale Italiana, Roma, Italy, [3]Dipartimento di Scienze della Terra, Università degli Studi di Firenze, Firenze, Italy, [4]Istituto di Geoscienze e Georisorse—IGG-CNR, Pisa, Italy, [5]Istituto di Astrofisica e Planetologia Spaziali—INAF, Roma, Italy, [6]School of Physical Science, The Open University, Milton Keynes, UK

Abstract We present a comprehensive study of a new Martian meteorite, Northwest Africa (NWA) 16788, found in the Sahara Desert in July 2023. This specimen constitutes the largest known individual meteorite of Martian origin, with a total weight of ~25 kg. A detailed mineralogical and geochemical investigation identifies NWA 16788 as an enriched olivine microgabbroic shergottite. Petrographic analysis reveals a millimeter-sized cumulate texture, which is intermediate between poikilitic and gabbroic shergottites, primarily composed of pyroxene (~61 vol.%), maskelynite (shocked plagioclase, ~21 vol.%), and olivine (~15 vol.%). Pyroxene grains exhibit a distinctive zoning pattern, placing NWA 16788 within a small group of Martian meteorites and lunar samples that record unique cooling histories, suggesting that similar samples may be more prevalent within the Martian igneous rocks than previously recognized. High-precision analyses of bulk $^{143}Nd/^{144}Nd$ and $^{87}Sr/^{86}Sr$ isotopic composition, combined with trace element abundance, indicate that NWA 16788 originated from the partial melting of an enriched Martian mantle source. Electron backscatter diffraction analysis reveals a unimodal distribution of olivine grain misorientation, averaging ~4.6°, consistent with a high-energy single-impact event. Moreover, visible and near-infrared spectroscopy data acquired on NWA 16788 could aid in identifying potential locations of analogous igneous rocks on the Martian surface. Finally, this study proposes refinements to the current classification scheme of Martian meteorites, aiming to reduce taxonomic ambiguity and improve the alignment between Martian meteorites and Martian igneous rocks, based on data from Mars rovers.

Plain Language Summary Martian meteorites provide direct insights into Mars' composition, geological processes, and evolutionary history. This study presents a comprehensive petrological, geochemical, and visible to near-infrared spectroscopic analysis of Northwest Africa (NWA) 16788, a new olivine microgabbroic shergottite distinguished by its unusually large size for a Martian meteorite. Our results reveal that NWA 16788 exhibits a distinctive pyroxene chemical evolution, linking it to a small group of Martian meteorites and lunar samples that record unique cooling histories. We suggest that such distinctive samples may be more distributed within Martian igneous rocks than previously recognized. Further investigation of this suite of Martian meteorites is crucial to advancing our understanding of the complexity of Mars' geological history.

Key Points:

- We present a comprehensive petrological and geochemical study of a new olivine microgabbroic shergottite, Northwest Africa 16788
- We suggest that similar samples may be more distributed within Martian igneous rocks than previously recognized
- New VNIR data of Northwest Africa 16788 may help identify potential sites containing similar igneous rocks on Mars

Supporting Information:

Supporting Information may be found in the online version of this article.

Correspondence to:

G. Pratesi,
giovanni.pratesi@unifi.it

Citation:

Shehaj, X., Pratesi, G., Carli, C., Avanzinelli, R., Stephant, A., Franza, A., & Ammannito, E. (2025). Northwest Africa 16788: The largest known individual Martian meteorite—A new Olivine microgabbroic shergottite and its implications for Martian magmatism. *Journal of Geophysical Research: Planets*, *130*, e2024JE008885. https://doi.org/10.1029/2024JE008885

Received 12 DEC 2024
Accepted 23 AUG 2025

1. Introduction

Martian meteorites are rocky fragments that originated on Mars, were ejected into space by asteroid impacts, and ultimately reached Earth as meteorites (Artemieva & Ivanov, 2004; Fritz et al., 2005; Herd et al., 2024; McSween, 1994). As the only samples currently available from Mars, these meteorites serve as essential records for reconstructing the history of Martian magmatism, mantle dynamics, and surface evolution (e.g., Borg & Drake, 2005; Debaille et al., 2007; Humayun et al., 2013; Papike et al., 2009). Martian meteorites are distinguished from other achondrites by their unique chemical, mineralogical, and isotopic signatures, which closely correspond with compositional data obtained from the Martian surface and atmosphere by spacecraft and rover missions such as Viking, Curiosity, and *Perseverance* (Bogard & Johnson, 1983; Bogart et al., 1984, 1986; Cousin et al., 2017; Liu et al., 2022; McSween, 1984; Wiens & Pepin, 1988).

These meteorites are traditionally classified into three groups: Shergottites (basalts in *sensu lato*), Nakhlites (olivine clinopyroxenites), and Chassignites (dunite), collectively referred to as SNC meteorites (e.g., Udry et al., 2020). In addition, unique types such as the orthopyroxenite ALH 84001 and regolith breccias, including NWA 7034 and its paired samples, have been identified (e.g., Agee et al., 2013; Mittlefehldt, 1994).

Similar to terrestrial basalts, Martian meteorites are further subdivided into enriched, intermediate, and depleted geochemical groups based on their rare earth element (REE) patterns, incompatible trace elements, and radiogenic isotopic compositions such as $^{143}Nd/^{144}Nd$ and $^{87}Sr/^{86}Sr$ (e.g., Symes et al., 2008; Udry et al., 2020, 2025). Shergottites represent the most abundant type by sample count, and are subdivided into basaltic (including augite-rich basalts such as NWA 7635 and NWA 8159), olivine-phyric, poikilitic, and gabbroic subtypes based on their petrography (Udry et al., 2020, and references therein). Basaltic and olivine-phyric shergottites are inferred to have crystallized in extrusive or near-surface environments, leading to fine-grained textures (e.g., Howarth & Udry, 2017; Howarth et al., 2018). In contrast, poikilitic (formerly termed lherzolitic) and gabbroic shergottites are interpreted to have crystallized in hypabyssal settings, where slower cooling allowed the growth of larger crystals (e.g., Benaroya et al., 2024; Combs et al., 2019; Filiberto et al., 2018; Kizovski et al., 2019). Poikilitic shergottites are primarily characterized by a bimodal texture consisting of large (>3 mm) pyroxene oikocrysts (host crystals) that contain olivine chadacrysts (included crystals) up to 1.8 mm in size, along with an interstitial non-poikilitic texture in which plagioclase (or maskelynite–shocked plagioclase–in most cases) abundance is typically less than 20 vol. % (Combs et al., 2019; Udry et al., 2020). Additionally, pyroxene shows a bimodal composition ranging from low-Ca to high-Ca pyroxene (e.g., Combs et al., 2019).

On the other hand, gabbroic and olivine-gabbroic shergottites are primarily characterized by a coarse-grained (typically ≥1 mm) cumulate texture composed of pyroxene, maskelynite, and olivine assemblages bearing marked textural resemblance to terrestrial gabbroid (Benaroya et al., 2024; Filiberto et al., 2014, 2018; Saper et al., 2025; Udry et al., 2017; Wu et al., 2023). Within this group, additional petrographic subdivisions have been proposed, including olivine microgabbroic varieties (Meteoritical Bulletin database, 2025). These lithologies are believed to have formed through the slow cooling of magma, possibly within the Martian crust, thus promoting the development of larger crystals (e.g., Benaroya et al., 2024; Filiberto et al., 2014, 2018). To date, about 5.4% of the total Martian meteorites are officially classified as (olivine-) gabbroic or (olivine-) microgabbroic shergottites (Meteoritical Bulletin Database, 2025). Despite their significance for understanding Martian magmatic evolution, gabbroic (Filiberto et al., 2014, 2018; Saper et al., 2025; Udry et al., 2017) and olivine-gabbroic (Benaroya et al., 2024; Irving et al., 2018; Righter et al., 2019; Wu et al., 2023) shergottites remain comparatively understudied relative to other Martian lithologies (e.g., Udry et al., 2020). In this study, we examine the petrography, mineralogy, reflectance spectroscopy, bulk chemical and isotopic composition of NWA 16788, a newly identified olivine microgabbroic shergottite. Our goal is to elucidate its petrogenesis and gain new insights into the magmatic and thermal history of the Martian crust.

2. Sample and Analytical Methods

2.1. Sample and Sample Preparation

Northwest Africa 16788 is a Martian meteorite classified as shergottite, discovered in July 2023 in the Sahara Desert near Kefkaf, Niger (Meteoritical Bulletin Database, 2025). With a total weight of ~24.67 kg, it represents the largest Martian meteorite recorded in the Meteoritical Bulletin Database to date (Franza et al., 2024). The main mass, illustrated in Figure 1a, comprises a single stone measuring approximately 38 × 27 × 15 centimeters (cm), covered by a reddish-brown fusion crust of variable thickness. Regmaglypts—small surface depressions formed by thermal ablation during the entry into Earth's atmosphere—are visible in the central and lower-right portions of the specimen (Figure 1a). Three cm-scale slices were analyzed in this study. The first (~3 cm^2) was embedded in epoxy resin and prepared as a polished thick section for electron microscope analyses, including SEM-EDS, -EBSD, and EMPA (Figure 1b). The second (~3 cm^2) was subdivided into two chips: one prepared as a thin section for petrographic investigation, and the other powdered (<50 μm) for bulk chemical and isotopic characterization as well as reflectance spectroscopy analyses. The third (>6 cm^2) was allocated exclusively for reflectance spectroscopy measurements.

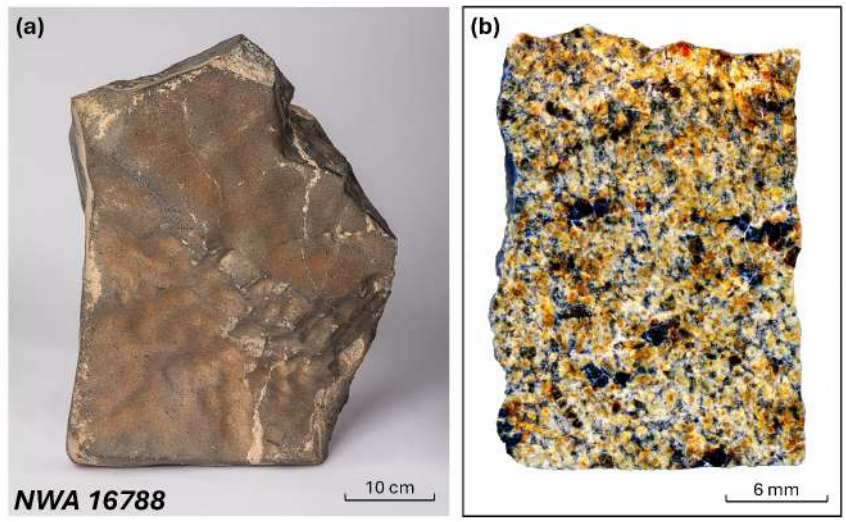

Figure 1. Photographs of the NWA 16788 Martian meteorite. (a) Full photograph representing the main mass specimen. (b) Incident light photograph of the thick, polished section.

2.2. SEM and Optical Microscope

The electron microscope measurements were conducted using a Zeiss EVO MA15 scanning electron microscope (SEM) equipped with a 40 mm^2 Silicon Drift Detector (SDD) and Oxford UltimMax, and data were processed using AZtec 5.1 microanalysis software at the Electron Microscopy and Microanalysis facility (MEMA) of the University of Firenze, Italy. Semiquantitative Energy Dispersive X-ray Spectroscopy (EDS) analyses were carried out at 15 kV acceleration voltage and 700 pA nominal beam current, with a spectrum count rate (cps) of 6,300, and acquisition livetime of 20 s, under high vacuum conditions (~$10^{(3}$ Pa). Semiquantitative chemical data were obtained from point analyses by converting count rates to concentrations, using energy and beam calibration on a pure Cobalt standard, and factory-based quantitative standardizations for the elements of interest. High-resolution elemental maps were acquired by EDS, operating at 15 kV accelerating potential and 700 pA probe currents, 54,000 as cps, and an acquisition livetime of 3,200 s. The sample was sputtered-coated with a 30-nm-thick carbon film. Mineral modal abundances were estimated by digitizing the BSE image using the *ImageJ* software. Thin sections were analyzed using a Zeiss Axioplan II optical microscope equipped with a Zeiss Axiocam camera.

2.3. EBSD

The sample was polished using 1 and 0.25 μm abrasive paste (SiC) before being further polished for 4 hr using 0.06 μm colloidal silica. The sample was cleaned in an ultrasonic bath for 10 min in 2-propanol to remove potential contaminants and then sputtered-coated with a 5-nm-thick carbon film. An Electron Backscattered Diffraction (EBSD) mapping was conducted using Zeiss EVO MA15 SEM coupled with a high-performance CMOS Oxford Symmetry S3 EBSD system located at the University of Firenze, Italy—MEMA laboratory. The analyses were performed at 15 kV and 9 nA nominal current, using a tilted angle mode (standard tilt angle of 70°). A step size of 12 μm was applied to map a rectangular area of 280 mm^2. Kikuchi patterns were collected by Oxford Instruments AZtecCrystal 3.1 software via automated Large Area Mapping and processed using Oxford Instruments HKL software Channel 5. The raw data were cleaned by wild-spike correction and iterative eight-point nearest neighbor zero solutions to minimize artifacts (e.g., Daly et al., 2019). Olivine data were used to generate the Grain Orientation Spread (GOS) map. Only grains larger than 70 μm in equivalent diameter ($GOS_{d>70}$) were considered to exclude misidentified grains, as olivine in NWA 16788 is typically larger than this threshold.

2.4. EMPA

Compositional quantitative point analyses were conducted using a JEOL JXA/8230 Electron Microprobe Analysis (EMPA) at LaMA, a joint UNIFI—IGG CNR laboratory at the University of Firenze, Italy. The sample

was sputtered-coated with a 30-nm-thick carbon film. Olivine, pyroxene, and oxide analyses were performed at 15 kV and 20 nA with an analytical spot size of 3 μm, while a defocused beam of 10 μm was used for maskelynite analyses. Phosphates, pyrrhotite, and melt inclusions were analyzed at 15 kV and 10 nA with a 10 μm spot size. The following crystals were used for element detection: Thallium Acid Phthalate (TAP) for Si, Al, Mg, and Na; Pentaerythritol (PET) and its variants (PETL, PETJ, PETH) for Ca, K, P, Ti, Sr, S, Ba, Cl, Nb; Lithium Fluoride (LIF) and LIFL for Fe, Mn, Cr, Ni, Co, Zn, and V; and a light-element artificial layered dispersive element (LED1) for F. The counting times for each element were 15 s on the peak and 7 s for each background. Natural and synthetic standards were used for wavelength dispersive spectrometry (WDS) included Albite (Si, Na), Ilmenite (Ti, Fe), Plagioclase (Al), Chromite (Cr), Bustamite (Mn), Pentlandite (Ni), Olivine (Mg), Diopside (Ca), Sanidine (K), Celestite (Sr, S), Apatite (P), Fluorite (F), Tugtupite (Cl), Sphalerite (Zn), Cobaltite (Co), Vanadium metal (V), Niobium metal (Nb), Willemite (Zn), Barite (Ba). The data were corrected for matrix effects using the ZAF method within the JEOL software package.

It should be noted that due to unknown crystallographic orientations of apatite grains, the quantification of F and Cl may be affected by anisotropic diffusion during EMPA measurements, as previously shown by Stormer et al. (1993). X-ray element maps (660 × 400 μm) were acquired in wavelength-dispersive mode for Mg Kα, Fe Kα, and Ca Kα using a focused 1 μm beam at 15 kV and 20 nA, with a step size of 4 μm and a dwell time of 500 ms per pixel.

2.5. Bulk Major and Minor Element Composition by EMPA Analysis

We estimated the bulk major and minor element compositions following the method outlined by Benaroya et al. (2024). Specifically, the bulk chemical composition was derived by integrating the quantitative mineral chemistry from EMPA point analyses with SEM-EBS and X-ray mapping (e.g., Benaroya et al., 2024; Gross et al., 2020). This approach assumes that the modal mineralogy, determined by abundance per unit area from SEM-EBS and X-ray maps, corresponds to abundance per unit volume under the assumption of a homogeneous mineral composition. The volume proportions were then converted into mass proportions for each mineral phase using density values reported by Smyth and McCormick (1995). The average EMPA point analysis for each mineral species was weighted by its mass-modal abundance. To mitigate the effects of compositional zoning, the modal abundances of pyroxene and olivine were adjusted for chemical zoning domains using X-ray chemical mapping. In particular, zoning domains were identified by combining high-resolution SEM-EDS and EMPA-WDS maps, specifically elemental maps of Mg, Ca, and Fe for pyroxene and olivine. Selected X-ray maps are shown in Figure S1 (Supporting Information S1). For pyroxene grains, we identified three domains: (a) Mg-rich pigeonite core, (b) augite mantle, and (c) Fe-rich pigeonite rim, while core and rim domains were identified for olivine grains. These images were processed using *ImageJ* software to track and quantify the zoning domains.

2.6. Bulk Chemical Composition by ICP-MS

A chip, approximately one cm in size and weighing 678.5 mg, was placed in a synthetic-glass beaker for the cleaning procedure. The sample was cleaned in an ultrasonic bath following a sequential protocol: (a) 10 min (min) in Ultra-Pure Water (MQ), (b) 10 min in 2-propanol, (c) 10 min in MQ, and (d) dried down for 12 hr (h) at 30°C in the laboratory oven. Following cleaning, the sample was manually ground into powder using an agate mortar and pestle. Three aliquots of the powdered sample (100 mg each) were weighed into pre-cleaned Teflon Savillex standard vials for the chemical dissolution procedure. The samples were digested in a 4:1 mixture of concentrated HF: HNO_3 at 140°C for 72 hr. Subsequently, the sample-acid solution was evaporated and treated with 2 mL HNO_3 at 140°C for 72 hr; this step was repeated twice. The samples were then evaporated again and subjected to reflux in HCl (6N) at 140°C for 48 hr, and finally evaporated. The resulting samples were divided into two aliquots: one designed for trace element analysis and the other for isotopic analysis. Trace element concentrations were determined from the HNO_3 sample solution using an Agilent 7800 (Agilent Technologies, Tokyo, Japan) Inductively Coupled Plasma—Mass Spectrometry (ICP-MS) at the Laboratory of Geochemistry of Radiogenic Isotopes—Earth Sciences Department, University of Firenze, Italy. Each of the three aliquots was analyzed twice. To assess the accuracy and precision of the chemical analyses, replicate measurements were performed on certified reference standard materials SRM987, NdFi, BHVO1, and AGV-1.

2.7. High-Precision Sr and Nd Isotopic Composition

The $^{87}Sr/^{86}Sr$ and $^{143}Nd/^{144}Nd$ isotope ratios were determined from aliquots derived from the same dissolution batches used for trace element analysis. Strontium and Nd were purified using a two-step conventional cation exchange chromatography protocol, following the procedure described by Avanzinelli et al. (2005). In the first step, Sr and REE were separated and collected using AG50Wx8 cation exchange resin (200–400 mesh, Bio-Rad®) located in 3.7 ml quart columns. In the second step, Nd was further isolated from the remaining REE using Ln-Resin (100–150 μm, Eichrom®) in 1 ml quartz columns. The bulk Sr and Nd isotopic compositions were measured by Thermal Ionization Mass Spectrometry (TIMS) using a Thermofisher Finnigan Triton Plus at the Laboratory of Geochemistry of Radiogenic Isotopes of the University of Firenze, Italy. Isotopic ratios were calculated as the average of multiple-cycle measurements to minimize the analytical error. Strontium isotopes were measured in multi-dynamic mode following the methodology of Thirlwall (1991) and Avanzinelli et al. (2005). Each analysis consisted of 120 cycles, each including three mass jumps (further details are reported in Avanzinelli et al., 2005). Neodymium analyses were measured in static mode involving 300 cycles organized into 30 blocks. During data acquisition, the connection between cups and amplifiers was switched alternately in a predefined sequence at the end of each block (virtual amplifier) to mitigate potential errors associated with amplifier gain calibration. An outlier test was performed to exclude values deviating from the average by more than $\pm 2\sigma$.

2.8. VNIR Reflectance Spectroscopy

Visible and near-infrared reflectance (VNIR) spectra of the NWA 16788 were acquired using a Fieldspec Pro spectrophotometer mounted on a goniometer at the S.LAB laboratory, part of the Institute of Space Astrophysics and Planetology (IAPS-INAF) in Rome, Italy. Reflectance measurements were conducted on both the powdered sample (<50 μm) and two areas on the surface of the meteorite slice (see Section 2.1 for further details). The samples analyzed for reflectance spectroscopy were designated as follows: NWA 16788 powdered, NWA 16788 slab area 1, and NWA 16788 slab area 2. For the powdered sample, five different spectra were collected and subsequently averaged to obtain the representative NWA 16788 powder spectrum. For NWA 16788 slab area 1, a total of 18 spectra were acquired over a 10×30 mm area, arranged in a 6X3 matrix, with a 0.4 mm step increment, and averaged accordingly. Additionally, two spectra were collected for NWA 16788 slab area 2, corresponding to a region of the NWA 16788 slab area 1 enriched in olivine crystals, and were averaged to obtain a representative spectrum for that area. The goniometer configuration enabled near-bidirectional reflectance measurements, following the setup described in Carli et al. (2018 and references therein). The spectra were acquired in the spectral range of 0.35–2.50 μm with a spectral resolution of 3 nm in the VIS and 10–12 nm in the NIR. Illumination and viewing angles were fixed at 30° and 0°, respectively. A quartz tungsten halogen lamp was used as the light source, and the illuminated spot had a diameter of about 6 mm. The standard reference calibration was performed using a Spectralon® 99% optical standard (Labsphere, Inc.). Spectral analysis was performed on the averaged spectra of NWA 16788. Continuum removal was applied to facilitate the evaluation of spectral indices. Each spectrum represented the average of 200 individual acquisitions. We analyzed the average spectra of NWA 16788 by evaluating the spectral indices after the continuum was removed. We calculated the continuum as the straight-line segments, a function of wavelength, which join the reflectance maxima in the spectrum (Clark & Roush, 1984). The band center was calculated as the wavelength positions corresponding to the minimum reflectance after continuum removal. The Band Area Ratio was determined as the integrated area between the continuum and the continuum-removed spectra, following Cloutis et al. (1986). For comparative analysis, the spectral properties of NWA 16788 were evaluated alongside published VNIR spectra of Martian meteorites reported by Mandon et al. (2021) and Filberto et al. (2018).

2.9. Oxygen Fugacity Calculation

The oxygen fugacity (fO_2) was estimated using two distinct thermodynamic approaches, each corresponding to different stages of magma crystallization. For the early crystallization stage, fO_2 was determined using the olivine-orthopyroxene-spinel (Ol-Opx-Spn) oxy-geothemobarometer developed through a series of thermodynamic models by Sack and Ghiorso (1989, 1991a, 1991b, 1994a, 1994b, 1994c) and subsequently refined by Benaroya (2023). This method is based on equilibrium relationships among coexisting olivine, orthopyroxene, and spinel. To ensure accurate estimations, only grains in textural and chemical equilibrium were selected by EMPA analyses following the criteria outlined by Benaroya et al. (2024). A pressure of 10 kbar was assumed for

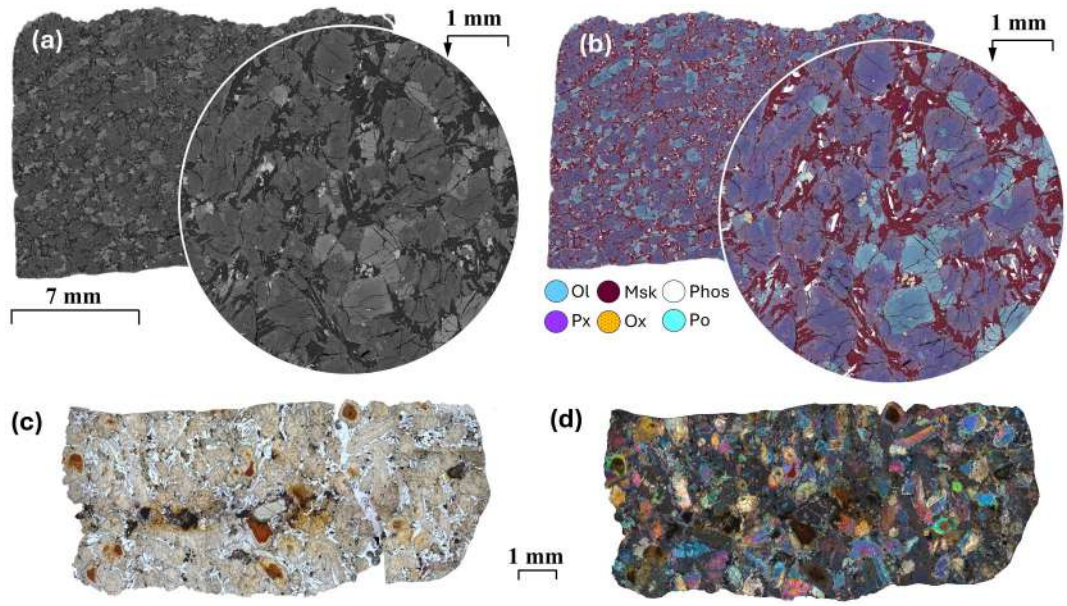

Figure 2. Backscattered electron (BSE) and optical microscope mosaics of NWA 16788. (a) Panoramic BSE and a zoomed portion of NWA 16788 thick section, and (b) combined X-ray maps generated by AZtec software. Mineral phases (Ol = olivine, Mks = maskelynite, Px = pyroxene, Phos = phosphates, Ox = oxides, Po = pyrrhotite) are identified by X-ray maps with the colors provided in the legend. (c) Panoramic mosaic of NWA 16788 thin section in plane polarized light and crossed polarized mode (d).

these calculations, consistent with constraints from previous studies (Benaroya et al., 2024; Combs et al., 2019; Filiberto et al., 2018). For the late crystallization stage, fO_2 was estimated using the Fe-Ti oxy-geothemobarometer developed by Ghiorso and Evans (2008), which relies on thermodynamic equilibrium between magnetite and ilmenite. This method is particularly sensitive to oxygen fugacity and provides insights into the redox conditions during the late state of the magmatic system. The chemical compositions of ilmenite and magnetite grains, confirmed to be in textural equilibrium, were measured via EMPA. The results obtained from the Ghiorso and Evans (2008) calculator, originally expressed relative to the Nickel–Nickel Oxide (NNO) buffer, were subsequently converted to the Quartz–Fayalite–Magnetite (QFM) buffer using the equation of Wones and Gilbert (1969).

3. Results

3.1. Petrography

3.1.1. Texture

Backscattered electron (BSE) images and optical mosaics reveal a millimeter-sized cumulate texture dominated by a homogeneous distribution of pyroxene (61.1 vol.%), maskelynite (i.e., shocked plagioclase, 21.2 vol.%), and olivine (15.3 vol.%) assemblages (Figure 2). Accessory phases include phosphates (1.4 vol.%), ilmenite + Fe-Cr-Ti oxides (0.8 vol.%), and pyrrhotite (0.2 vol.%) (Figures 2–4). A poikilitic texture with olivine chadacrysts (~100 μm) enclosed by pyroxene oikocrysts (from 1 to 2.5 mm) is also observed (Figures 3a and 3e). Pyroxene, olivine, and accessory phases exhibit numerous irregular cracks and fractures. A set of fractures oriented perpendicular to the elongate axes appears in pyroxene and olivine grains. Micrometric veins enriched in Ca-carbonate, likely resulting from terrestrial weathering, are found around shock-melt pockets (Figure 5a).

3.1.2. Pyroxene

Pyroxenes, the most abundant phase in NWA 16788, are generally equant in size ranging from approximately 0.5 and 1 mm, averaging around 0.7 mm, with some crystals reaching lengths up to 2.7 mm. These grains are mainly subhedral with granular or lath-like textures (Figures 2 and 3), and usually elongate to the c-axis. Pyroxene exhibits complex zoning patterns including oscillatory and concentric zoning (Figure S1 in Supporting

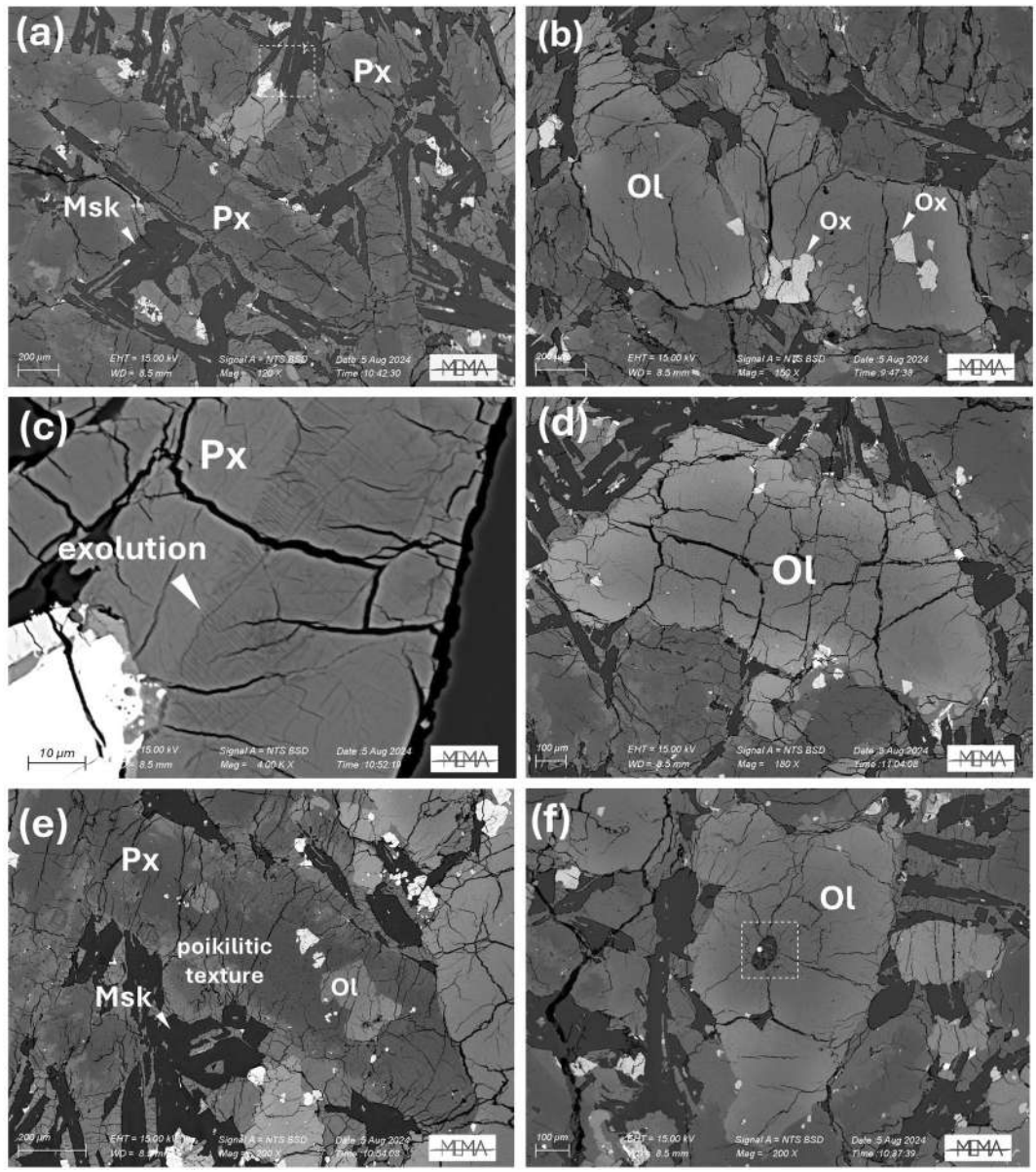

Figure 3. High magnification BSE images of texture and mineralogy in NWA 16788. (a) Lath-like texture of pyroxene (Px) and maskelynite (Msk) grains. (b) Olivine (Ol) grain with oxide (Ox) inclusion. (c) Pyroxene exsolution lamellae (a zoomed portion of the highlighted rectangle in a). (d) Euhedral olivine grain. (e) Poikilitic texture with olivine chadacryst enclosed in pyroxene oikocryst. (f) Olivine grains with melt inclusion.

Information S1). Despite this, core, mantle, and rim domains are typically discernible in each grain, as illustrated in the pyroxene diagram and WDS chemical elemental maps (Figures 6 and 7). The average chemical compositions of the pyroxene core, mantle, and rim are reported in Table 1. Crystals show a progressive chemical evolution starting from an Mg-rich pigeonite core ($En_{67}Fs_{27}Wo_6$) mantled by augite ($En_{48}Fs_{32}Wo_{20}$) and rimmed by Fe-rich pigeonite ($En_{41}Fs_{46}Wo_{13}$) that extends into surrounding grains (Figure 7). In addition, significant chemical evolution is observed for Al, Ti, and Cr, as shown in the ternary diagram in Figure 6b. Magnesium-rich pigeonite core, enriched in Al and Cr [Σ(Al,Cr) $\approx$ 0.93; average expressed as the sum of Al, Cr, and Ti atoms per formula unit (apfu) normalized to 1], evolve to slight Ti enriched mantle [Σ(Al,Cr) $\approx$ 0.87] up to high Ti rim [Σ(Al,Cr) $\approx$ 0.75]. The pyroxene Ti/Al ratio remains constant (~0.15 apfu) from the Mg-rich core to the Ca-rich mantle but varies significantly in the Fe-rich rim (~0.35 apfu) and at certain mantle points (Figure S2 in Supporting Information S1). The pyroxene composition in NWA 16788 exhibits marked affinities with gabbroic and

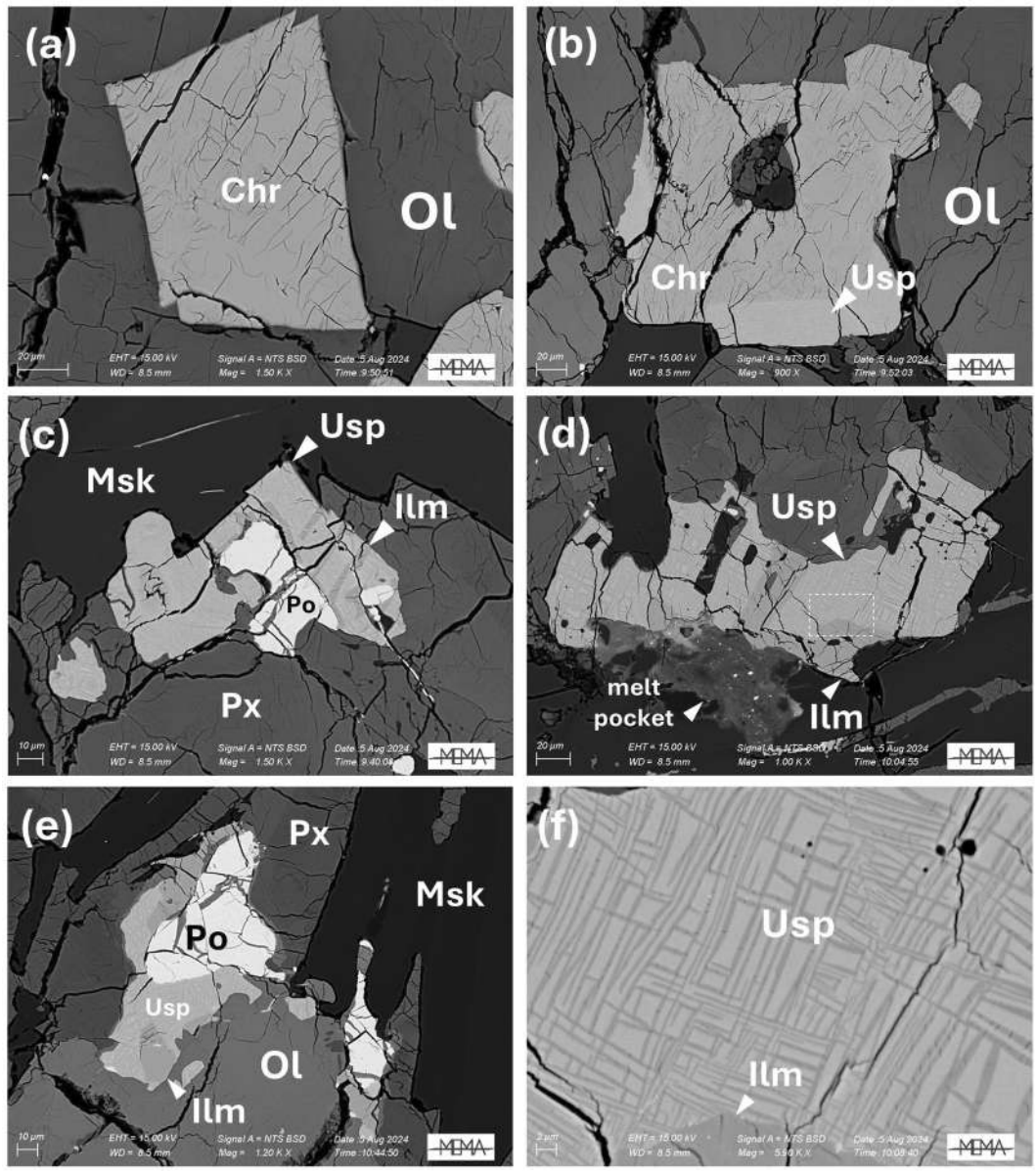

Figure 4. Backscattered electron images of oxides and pyrrhotite grains found in NWA 16788. (a) Chromite (Chr) enclosed in an olivine (Ol) grain. (b) Zoned chromite found at the edge of an olivine grain. (c, d, e) Ulvöspinel (Usp) oxides with ilmenite (Ilm) intergrowth and pyrrhotite. (f) Zoomed portion (highlighted in d) of ulvöspinel oxide with ilmenite exsolution lamellae.

olivine-gabbroic shergottites rather than poikilitic shergottites, which typically display a bimodal pyroxene composition (Figure 6a). Exsolution lamellae (a few hundred nm in width) were observed within some Fe-rich pigeonite rims (Figure 3c), although these features are below the resolution limit of a conventional scanning electron microscope.

3.1.3. Maskelynite

Maskelynite is the second most prevalent phase in NWA 16788, accounting for 21.2 vol % of the modal abundance. The presence of maskelynite, which is the conversion of feldspar to a diaplectic glass due to shock metamorphism, was confirmed via optical microscopy. Maskelynite commonly occurs as sub-millimeter (0.5 mm up to 1.2 mm in size) lath-like or prismatic grains (Figures 2 and 3), showing a homogeneous chemical

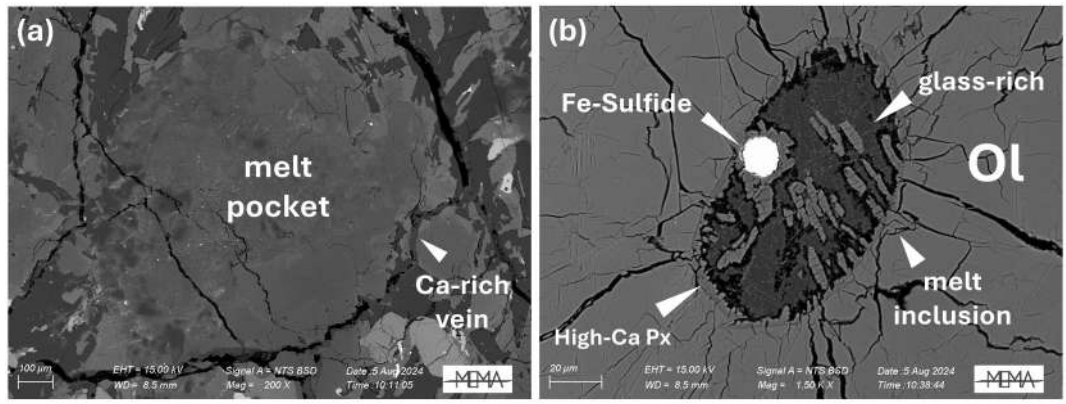

Figure 5. Melt pocket texture surrounded by fractures and Ca-rich veins (a), and a melt inclusion (b). The latter is a magnified view of the highlighted rectangle in Figure 3f.

composition with an average (avg.) of $An_{48}Ab_{49}$ (Table 1). These grains are frequently associated with phosphates, oxides, and pyrrhotite (Figure 4).

3.1.4. Olivine

Olivine, with a modal abundance of 15.3 vol.%, occurs both as isolated crystals and chadacrysts (Figures 2 and 3). The isolated euhedral-subhedral crystals range from ~70 μm to 2.8 mm in size, typically >0.5 mm (Figures 3b, 3d, and 3f). They usually show normal zoning from the Mg-rich core (avg. Fo_{56}) to the Fe-rich rim (avg. Fo_{47}). Early-formed euhedral olivine grains show more pronounced chemical zoning (e.g., core-Fo_{70} and rim-Fo_{46}) than late-formed anhedral grains (e.g., $Fo_{50\text{-}44}$). Generally, the MnO and TiO_2 content increases from core to rim, correlating with a decrease in CaO and NiO (Table 1). In contrast, olivine chadacrysts, enclosed in pyroxene oikocrysts, are distinguished by shape (reabsorption circular edges) and CaO content (depleted in CaO = 0.27 wt.%) compared to isolated grains (Figures 3e and 8). Primitive euhedral olivine grains often contain circular melt-inclusions consisting of polymineralic aggregates composed of high-Ca pyroxene, Fe-sulfide droplets, and small brightness inclusions in BSE mode (<1 μm)—possibly oxide grains, embedded in a (Si,Al)-rich glass (Figure 5b).

3.1.5. Accessory Phases

Accessory phases of NWA 16788 mainly comprise phosphates (1.4 vol.%), oxides (0.8 vol.%), and pyrrhotite (0.2 vol.%) (Figures 2 and 4). Phosphates commonly occur as prismatic or elongate acicular crystals ranging from 10 μm up to 600 μm in size. Electron microprobe analyses reveal two distinct mineral types: apatite and merrillite (Table 2). They are typically associated with maskelynite grains or with other accessory phases, such as oxides and pyrrhotite. The spinel structural group, expressed as a solid solution of chromite, magnetite, spinel, and ulvöspinel end-members, represents the most important oxide phase (Table 3). However, chromite and ulvöspinel members are the most abundant (Figure 9). Chromite occurs as homogeneous euhedral inclusions (typically >50 μm) with Cr# = 0.87 ± 0.02 [where Cr# is the molar Cr/(Cr + Al)], found within large olivine and pyroxene grains (e.g., Figure 4a) or at the boundaries of mafic silicates with ulvöspinel rims (Figure 4b). Anhedral aggregates of ulvöspinel, ilmenite, and pyrrhotite are commonly found in interstitial cavities (Figures 4c–4f). Ilmenite is associated with ulvöspinel as thin exsolution lamellae (~500 nm) or homogeneous grains (Figures 4d and 4f). The chemical composition of Fe-sulfide reveals an iron deficiency ($Fe_{0.88}S$) with a stochiometric formula corresponding to pyrrhotite (Table 2). Pyrrhotite forms anhedral grains, typically larger than 30 μm, surrounded by ulvöspinel and ilmenite oxides.

3.2. Shock Metamorphism

Shock metamorphism has been examined using semi-quantitative (optical microscopy, Stöffler et al., 2018, and references therein) and quantitative techniques, such as SEM-EBSD (Ruzicka & Hugo, 2018).

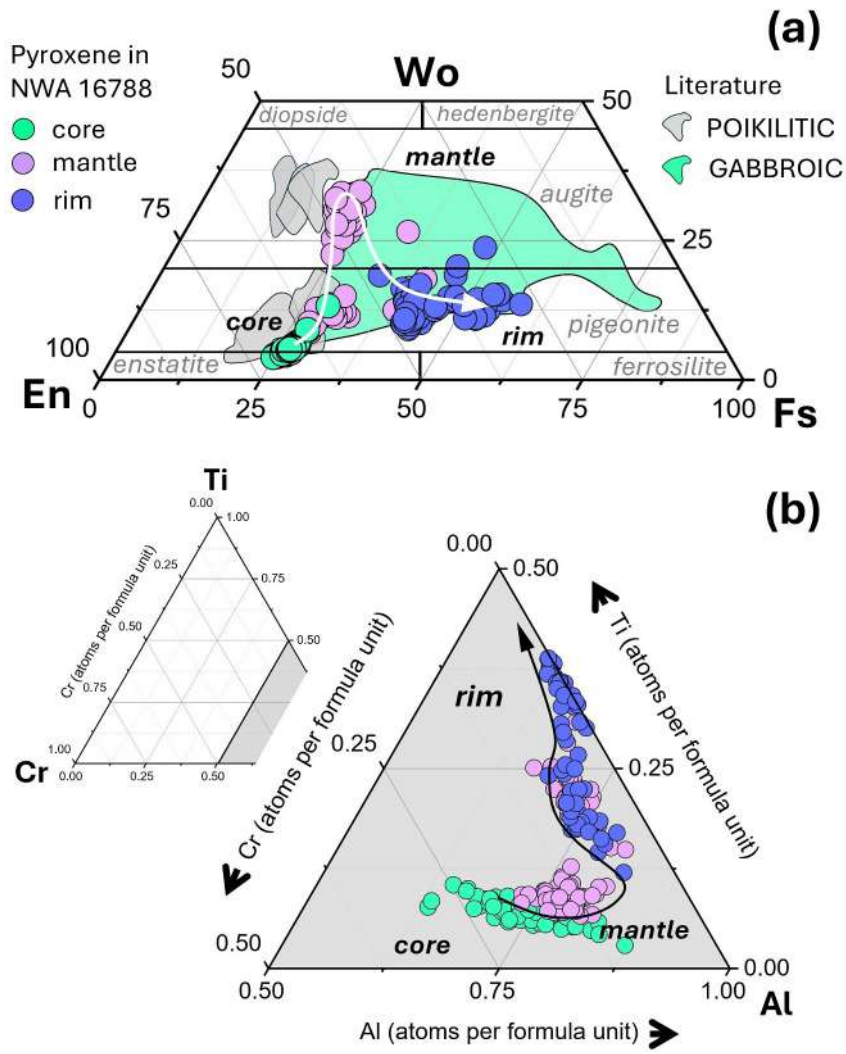

Figure 6. Pyroxene composition in NWA 16788. (a) Quadrilateral pyroxene diagram of the NWA 16788 compared with the zoning field of poikilitic, gabbroic and olivine-gabbroic shergottites (literature data from Benaroya et al. (2024), Filiberlo et al. (2018), Liu et al. (2022), Saper et al. (2025), and Udry et al. (2017)). The pyroxene zoning trends of NWA 16788 are indicated by the white arrow. End-member components are expressed as follows: Wo = Wollastonite ($CaSiO_3$), En = Enstatite ($MgSiO_3$), Fs = Ferrosilite ($FeSiO_3$). (b) Cr-Al-Ti ternary diagram of pyroxene composition. The black arrow indicates the zoning trend.

3.2.1. Optical Microscopy Analysis

The shock grade deformation was estimated using the optical microscopy method proposed by Jamsja and Ruzicka (2010). Each olivine grain larger than 70 μm was assigned a shock stage on a scale from 1 (weakly shocked) to 6 (highly shocked), and the average value was calculated to obtain a "weighted" or "mean shock stage," following the approach outlined by Stöffler et al. (1991), Jamsja and Ruzicka (2010), and Friedrich et al. (2017). Olivine grains commonly exhibit planar deformation features (PDFs), varying degrees of mosaicism (from weak to strong) and, in some cases, a yellow-brown stained core (Figure 10). Based on these features, we estimated a "weighted shock stage" of 4.85 ± 0.87 (1σ for 55 values) for NWA 16788 (Figure 11a). In addition, the absence of birefringence in the plagioclase grains indicates complete maskelynitization (Figures 2c, 2d, 10a, and 10b). Shock-induced melt pockets were also identified (Figure 10c). Collectively, these characteristics are consistent with a shock grade of S5 according to the scheme proposed by Stöffler et al. (1991).

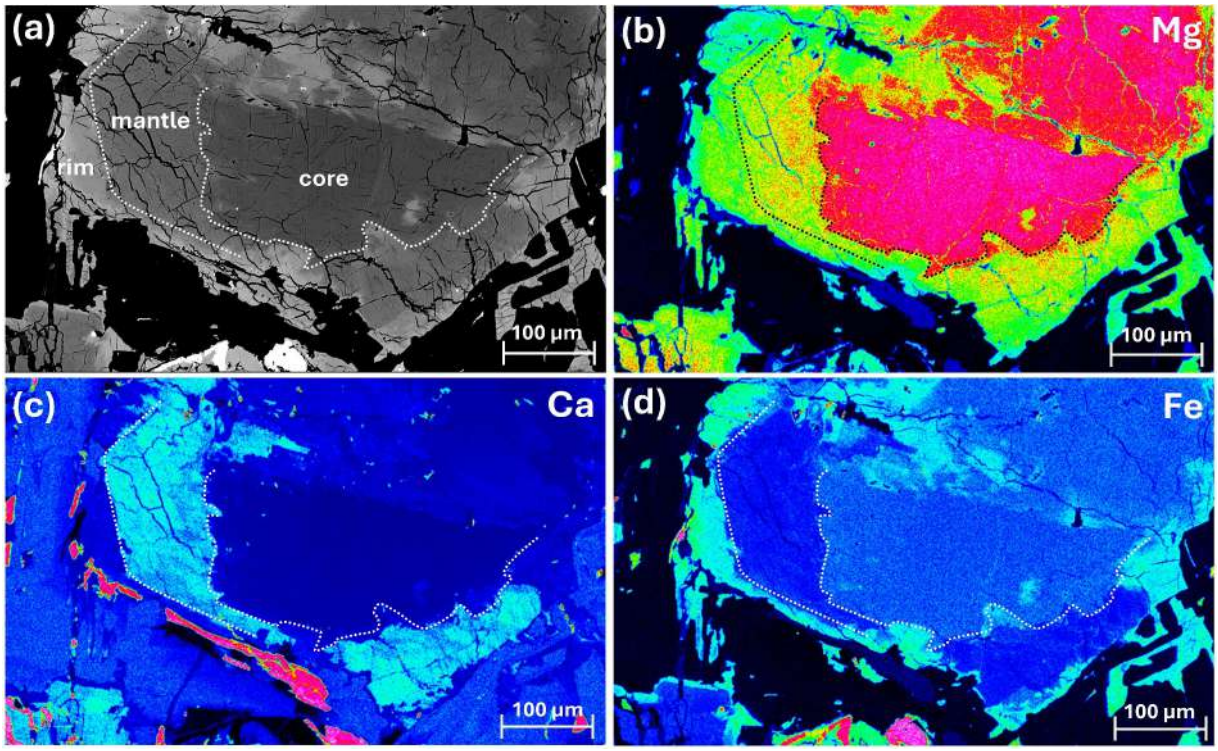

Figure 7. Backscattered electron image (a) and X-ray elemental maps in WDS mode of the pyroxene chemical zoning domain for Mg Kα (b), Ca Kα (c), and Fe Kα (d) in NWA 16788. The map uses a warm-to-cold color scale, where warmer colors indicate higher concentrations and cooler colors indicate lower concentrations.

3.2.2. Electron Microscope Analysis (SEM-EBSD)

Recent studies have proposed that the GOS value, defined as the average misorientation angle for each grain, can serve as a quantitative proxy for assessing the shock stage deformation induced by impact processes (e.g., Ruzicka & Hugo, 2018). In this context, we mapped the olivine grains' GOS value for NWA 16788 (Figures 11b and 11c), which shows a unimodal distribution and an average $GOS_{d>70}$ value of 4.69° ± 1.07 (1σ for 889 values). This result is consistent with the petrographic weight shock stage (4.85 ± 0.87) previously estimated through optical microscopy (Figure 11a).

3.3. Geochemistry

The major, minor, and trace bulk chemical abundances of NWA 16788 are reported in Table 4. The major abundances estimated through EMPA analyses are consistent with those measured by ICP-MS (Table 4). The chemical composition of the NWA 16788 aligns with the gabbroic and olivine-gabbroic shergottites as well as the enriched shergottites geochemical group as shown in Table 4 and Figure 12. The bulk Mg# = 56 [where Mg# is the molar Mg/(Mg + Fe) × 100] and CaO wt.% (6.27 ± 1.45) indicate a permafic composition, according to Irving et al. (2010). The rare earth elements (REE) pattern, normalized to CI-chondrite (Lodders, 2003), is relatively flat with a $(La/Yb)_{CI}$ ratio of 1.09 (Figure 12a). The trace element pattern shows a relatively high abundance of fluid-mobile elements (e.g., Ba and Sr; Figure 12b). Both diagrams show significant overlap with the olivine-gabbroic shergottite field. Isotopic analysis of Nd and Sr (Table 4) reveals a high $^{87}Sr/^{86}Sr$ ratio (0.719444 ± 5) and low $^{143}Nd/^{144}Nd$ ratio (0.512282 ± 1), consistent with the enriched shergottite geochemical group (e.g., Borg & Draper, 2003; Borg et al., 2002; Day et al., 2018).

3.4. Reflectance Spectroscopy

Reflectance spectra acquired on NWA 16788 are dominated by pyroxene absorption features, particularly near 1 µm (Band Center I, BC1) and 2 µm (Band Center II, BC2), as shown in Figure 13. While powder and slab area 1

Table 1
Average Element Composition of Silicate Grains Expressed in Oxide Weight Percentage (wt.%), and 1σ Standard Deviation

	Pyroxene						Olivine						Maskelynite	
	Core		Mantle		Rim		Core		Rim		Chadacryst			
Silicates Texture	Avg. (91)[a]	1σ	Avg. (102)	1σ	Avg. (73)	1σ	Avg. (105)	1σ	Avg. (115)	1σ	Avg. (49)	1σ	Avg. (65)	1σ
ox. wt.%														
SiO_2	53.73	*0.54*	51.50	*1.03*	50.08	*0.78*	35.48	*1.01*	34.27	*0.84*	35.67	*0.91*	56.28	*1.06*
TiO_2	0.12	*0.04*	0.34	*0.11*	0.52	*0.13*	0.03	*0.01*	0.04	*0.02*	0.04	*0.01*	0.09	*0.01*
Al_2O_3	0.79	*0.19*	1.35	*0.50*	0.91	*0.25*	0.12	*0.12*	0.07	*0.10*	0.09	*0.11*	27.51	*0.46*
Cr_2O_3	0.43	*0.07*	0.42	*0.23*	0.12	*0.10*	0.06	*0.03*	0.04	*0.07*	0.05	*0.04*	n.d.	-
FeO	16.83	*0.98*	19.15	*5.06*	26.69	*2.68*	36.14	*5.18*	42.38	*4.19*	36.10	*4.54*	0.75	*0.13*
MnO	0.55	*0.04*	0.60	*0.11*	0.78	*0.09*	0.67	*0.09*	0.79	*0.08*	0.69	*0.08*	0.01	*0.01*
MgO	23.88	*1.18*	16.33	*2.04*	13.58	*2.09*	26.81	*4.12*	21.91	*3.51*	26.61	*3.75*	0.11	*0.04*
NiO	n.d.[b]	-	n.d.	-	n.d.	-	0.06	*0.02*	0.04	*0.02*	0.05	*0.02*	n.d.	-
CaO	2.75	*0.65*	9.29	*4.07*	6.04	*1.14*	0.34	*0.05*	0.30	*0.04*	0.27	*0.04*	9.74	*0.58*
Na_2O	0.05	*0.01*	0.13	*0.05*	0.08	*0.02*	n.d.	-	n.d.	-	n.d.	-	5.52	*0.31*
K_2O	0.03	*0.03*	0.01	*0.01*	0.01	*0.01*	n.d.	-	n.d.	-	n.d.	-	0.39	*0.08*
SrO	n.d.	-	n.d.	-	n.d.	-	n.d.	-	n.d.	-	n.d.	-	0.04	*0.02*
BaO	n.d.	-	n.d.	-	n.d.	-	n.d.	-	n.d.	-	n.d.	-	0.05	*0.01*
total	99.16	*0.39*	99.12	*0.43*	98.81	*0.40*	99.71	*0.68*	99.85	*0.53*	99.57	*0.63*	100.48	*0.70*
			norm. to 6 oxygen						*norm. to 4 oxygen*				*norm. to 8 oxygen*	
Si	1.981		1.964		1.971		0.996		0.994		1.002		2.527	
Al	0.034		0.060		0.042		0.004		0.002		0.003		1.456	
Ti	0.003		0.010		0.015		0.001		0.001		0.001		0.003	
Cr	0.008		0.008		0.003		0.001		0.001		0.001		-	
Mg	1.313		0.925		0.795		1.119		0.944		1.111		0.007	
Mn	0.017		0.020		0.026		0.016		0.019		0.016		<0.001	
Ni	-		-		-		0.001		0.001		0.001		-	
Fe^{2+}	0.519		0.613		0.880		0.852		1.031		0.851		0.028	
Ca	0.109		0.380		0.255		0.010		0.009		0.008		0.469	
Na	0.004		0.009		0.006		-		-		-		0.480	
K	0.001		0.001		0.000		-		-		-		0.022	
Sr	-		-		-		-		-		-		<0.001	
Ba	-		-		-		-		-		-		<0.001	
total	3.990		3.991		3.993		3.001		3.003		2.995		4.992	
En[c]	67.6		48.2		41.2		-		-		-		-	
Fs	26.8		31.9		45.6		-		-		-		-	
Wo	5.6		19.9		13.2		-		-		-		-	
Mg#	71.6		60.7		47.4		-		-		-		-	
Fo	-		-		-		56.2		47.2		56.1		-	
Fa	-		-		-		42.7		51.5		43.0		-	
La	-		-		-		0.5		0.5		0.4		-	
Tp	-		-		-		0.8		1.0		0.8		-	
An	-		-		-		-		-		-		48.3	

Table 1
Continued

	Pyroxene						Olivine						Maskelynite	
	Core		Mantle		Rim		Core		Rim		Chadacryst			
Silicates Texture	Avg. (91)[a]	1σ	Avg. (102)	1σ	Avg. (73)	1σ	Avg. (105)	1σ	Avg. (115)	1σ	Avg. (49)	1σ	Avg. (65)	1σ
Ab	-		-		-		-		-		-		49.4	
Or	-		-		-		-		-		-		2.3	

Note. Italics are referred to as error. [a]Avg. (average). [b]n.d. = non-determined. [c]En = enstatite, Fs = ferrosilite, Wo = wollastonite, molar Mg# = [Mg/(Mg + Fe^{2+})]100, Fo = forsterite, Fa = fayalite, La = larnite, Tp = tephroite, An = anorthite, Ab = albite, Or = orthoclase.

spectra exhibit a consistent pyroxene signature, the slab area 2 displays a slight shift of BC1 to longer wavelengths and a weaker band depth 2, consistent with the localized abundance of olivine crystals.

The comparison of band positions confirms that NWA 16788 aligns with the spectral trend characteristic of pyroxene (Figure 14) based on band parameters derived from synthetic pyroxenes as modeled by Burbine et al. (2018). Powder and slab area 1 show broadly comparable spectra parameters. However, in slab area 2, BC1 exhibits a shift toward higher values relative to the pyroxene trend.

Evidence of terrestrial alteration is minimal, limited to a weak absorption feature near 1.9 μm—indicative of an H_2O overtone on the slab surface—which slightly affects the BC2 position of pyroxene. However, this feature is not detectable in the powdered spectra due to the low abundance of hydrated secondary phases.

BC1 has been plotted against the Band Area Ratio (BAR), a spectral representation used to assess the relative abundances of olivine and pyroxene (Figure 15). Northwest Africa 16788 displays coherent values for both slab and powder spectra, with shifts toward higher BC1 and lower BAR in olivine-rich regions. This difference indicates spectroscopic variability at the analytical scale observed in the olivine microgabbroic lithology of NWA 16788. For reference, the olivine—orthopyroxene (ol-opx) mixing line from Gaffey et al. (1993), based on Cloutis et al. (1986), is included in Figure 15.

To further contextualize these results, we calculated BC1 and BAR values for powdered Martian meteorite spectra acquired under comparable illumination geometries (phase angle 30°; incidence/emission = 0°/30° or 30°/0°) as reported by Mandon et al. (2021). These data confirm that Martian meteorites, including NWA 16788, generally plot to the right of the ol-opx line (Figure 15), overlapping with fields occupied by other basaltic achondrites such as eucrites (Carli et al., 2022 and references therein).

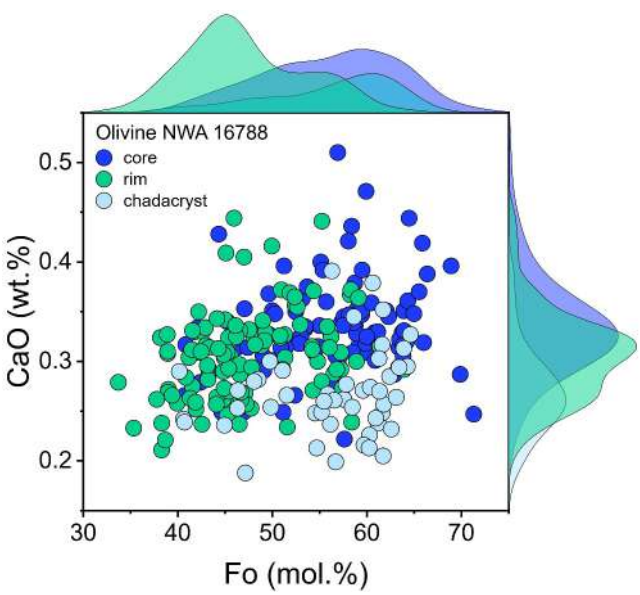

Figure 8. Forsterite (mole%) versus CaO (weight%) of olivine grains in NWA 16788.

4. Discussion

4.1. Northwest Africa 16788 Classification and Considerations About Classification Terms

The petrography of NWA 16788 reveals marked similarities to that of NWA 13227, an olivine-gabbroic shergottite. Both meteorites show an intermediate texture between gabbroic and poikilitic shergottites, dominated by pyroxene, maskelynite, and olivine with a cumulated texture. However, the two samples differ in grain size, with pyroxene grains in NWA 16788 appearing to be smaller (0.5–2.7 mm) than those in NWA 13227 (0.5–5 mm; Benaroya et al., 2024).

At present, no standardized size ranges have been established to clearly differentiate coarse-grained from fine-grained textures, such as those found in basaltic, microgabbroic, and gabbroic shergottites. Indeed, terms such as shergottite basalt, olivine-phyric, poikilitic, and gabbroic are applied inconsistently across the literature. For instance, NWA 12241 has been described both as a poikilitic olivine-gabbro (Nicklas et al., 2021) and a poikilitic

Table 2
Average Element Composition of Melt Inclusion and Phosphates Expressed in Oxide Weight Percentage (wt.%), and 1σ Standard Deviation

	Melt inclusion		Phosphates				Pyrrhotite	
			Merrillite		Apatite			
Phases	Avg. (4)	1σ	Avg. (9)	1σ	Avg. (4)	1σ	Avg. (11)	1σ
ox. wt.%								
SiO_2	66.76	*0.41*	0.37	*0.28*	0.57	*0.32*	0.02	*0.04*
TiO_2	0.62	*0.04*	n.d.	-	n.d.	-	0.14	*0.08*
Al_2O_3	18.14	*0.13*	n.d.	-	n.d.	-	0.01	*0.01*
FeO	1.15	*0.15*	2.52	*0.33*	1.06	*0.24*	58.63	*0.38*
NiO	n.d.[a]	-	n.d.	-	n.d.	-	0.75	*0.14*
CoO	n.d.	-	n.d.	-	n.d.	-	0.12	*0.01*
Cr_2O_3	n.d.	-	n.d.	-	n.d.	-	0.07	*0.06*
ZnO	n.d.	-	n.d.	-	n.d.	-	0.00	*0.01*
MnO	0.03	*0.02*	n.d.	-	n.d.	-	0.02	*0.02*
MgO	0.14	*0.02*	2.27	*0.18*	0.12	*0.07*	0.00	*0.00*
CaO	2.26	*0.23*	47.40	*0.35*	53.86	*0.39*	0.05	*0.04*
Na_2O	2.70	*0.07*	1.55	*0.13*	0.10	*0.05*	0.01	*0.02*
K_2O	7.14	*0.11*	n.d.	-	n.d.	-	n.d.	-
P_2O_5	0.71	*0.04*	45.35	*0.46*	41.74	*0.45*	0.00	*0.01*
SO_3	0.00	*0.00*	0.01	*0.01*	0.06	*0.02*	38.06	*0.43*
SrO	n.d.	-	0.03	*0.02*	0.02	*0.03*	n.d.	-
Cl	0.01	*0.01*	0.05	*0.09*	1.11	*0.44*	n.d.	-
F	0.11	*0.01*	0.11	*0.17*	1.97	*0.07*	n.d.	-
Total	99.79	*0.49*	99.67	*0.33*	100.61	*0.36*	97.89	*0.51*

Note. Pyrrhotite grains are expressed as elements weight percentages. Italics are referred to as error. [a]n.d. = non-determined.

shergottite (Benaroya et al., 2024 and references therein); Los Angeles and NWA 480 basaltic shergottites have been referred to as "microgabbro" and "gabbroic rock," respectively (Barrat et al., 2002; Xirouchakis et al., 2002), while the term "diabase" is frequently applied to some basaltic shergottites (Brearley, 1991; McFarlane & Spray, 2022; Nyquist et al., 2009; Udry et al., 2020). Furthermore, the term "lherzolitic shergottite" is now referred to as "poikilitic shergottite" (Udry et al., 2020).

In the terrestrial setting, gabbroic rocks—gabbros in *sensu lato*—are typically designed as coarse-grained (>3 mm), low cooling-rate mafic rocks dominated by pyroxene-plagioclase assemblages, with variable amounts of olivine, hornblende, and accessory minerals (Le Maitre et al., 2002). Diabase, dolerite, and microgabbro (fine-grained gabbro) are generally used synonymously (Le Maitre et al., 2002). Moreover, contrary to shergottites, the terms poikilitic and gabbroic are ubiquitous in terrestrial rocks because gabbroic suites can also have a poikilitic texture (e.g., Boulanger et al., 2021; Fodor & Moore, 1994). Furthermore, gabbros are chemically equivalent to the fine-grained (<1 mm), high cooling-rate basalts and are distinguished from ultramafic rocks (e.g., lherzolites) based on their mafic mineral content (<90 vol.%, Le Maitre et al., 2002). However, this distinction appears less evident in Martian meteorites, possibly due to missing samples in our collection (Herd et al., 2024) or the intrinsic nature of Martian geology (e.g., Filiberto et al., 2014).

Nevertheless, as illustrated in Figure 16, a terrestrial-like classification approach has been widely adopted in the literature for Martian meteorites as well as for interpreting petrographic data acquired by Martian rovers (Cousin et al., 2017; Day et al., 2018; Deng et al., 2020; Humayun et al., 2013; Liu et al., 2022; Malarewicz et al., 2025; Mangold et al., 2017; McSween et al., 2009; Sautter et al., 2016). A prominent example of terrestrial-like classification applied to Martian rocks is the use of the Total Alkali-Silica (TAS) diagram (Figure 16c), which was originally developed to classify terrestrial volcanic rocks based on their bulk chemical composition (Le Maitre et al., 2002). However, its application should be restricted primarily to high-cooling-rate extrusive volcanic rocks—such as basaltic, olivine-phyric, and augite-rich shergottites—as the TAS diagram was specifically designed for volcanic rock types (Le Maitre et al., 2002). Moreover, given the uncertain geological context of Martian meteorites—specifically, whether they originate from volcanic or plutonic settings—we propose the use, from this point onward, of the terms "volcanic-like" and "plutonic-like" to enable comparison with the terrestrial igneous classification system. More recently, the TAS diagram has also been extended to the classification of Martian plutonic-like lithologies, such as granitoids identified in Martian meteorites (Figure 16d). In this regard, TAS has been applied to identify and characterize granitoid lithologies within the regolith breccia NWA 7533 (Malarewicz et al., 2025). Nonetheless, the TAS diagram remains unsuitable for classifying low-cooling-rate plutonic-like mafic and ultramafic rocks, common lithologies among Martian meteorites (Udry et al., 2020). To address this limitation, alternative classification approaches have been employed, including modal and mineralogical schemes (Figure 16e). These have been applied to plutonic-like ultramafic Martian meteorites such as chassignites, nakhlites, ALH 84001, and poikilitic shergottites, as well as to complementary rover-derived data (Liu et al., 2022). In this study, we further explored this approach by plotting the gabbroic shergottite suite, including NWA 16788, using a modal classification framework (Figure 16f). These methods emphasize the compositional and textural diversity within Martian igneous rocks and provide a more appropriate way to characterize slowly cooled plutonic-like mafic and ultramafic lithologies.

The discovery of NWA 16788 highlights the increasing prevalence of intermediate samples that bridge the gap between gabbroic and poikilitic shergottites. This trend suggests that the current Martian classification framework is incomplete and more complex than typically envisioned (Figure 16). The proposal of intermediate petrographic terms to link gabbroic and poikilitic shergottites reflects this growing complexity (Benaroya et al., 2022). As new meteorites are recovered and studied (e.g., Herd et al., 2024; Malarewicz et al., 2025), it becomes evident that the

Table 3
Chemical Composition (wt.%) of Selected Fe-Cr-Ti Oxides

Fe-Cr-Ti-oxides[a]	Chr		Chr	Ulp	Mgt	Ulp	Ulp	Ulp	Ilm
Occurrence	Mafic silicate inclusion		Mafic silicate edge		Mafic silicates edge				
Texture	Homogeneous		Core	Rim	Exolution lamellae or single grains				
ox. wt.%									
SiO_2	0.10	0.10	0.09	0.04	0.13	0.08	0.08	0.05	0.00
TiO_2	0.58	0.61	0.64	19.95	11.75	22.67	22.13	24.44	49.81
Al_2O_3	6.72	6.46	6.59	3.34	2.51	1.63	2.35	2.16	0.06
V_2O_3	0.34	0.33	0.34	0.61	0.48	0.20	0.78	0.47	0.25
Cr_2O_3	58.37	58.19	56.17	17.29	0.79	0.11	1.86	2.55	0.10
FeO	27.39	27.33	30.82	51.86	80.51	70.75	67.99	65.21	46.89
MnO	0.50	0.49	0.48	0.60	0.34	0.53	0.49	0.52	0.74
NiO	0.04	0.03	0.04	0.04	0.02	0.02	0.00	0.03	0.00
MgO	4.60	4.73	2.75	1.76	0.35	0.56	0.69	0.86	1.04
CaO	0.02	0.00	0.00	0.03	0.06	0.05	0.09	0.10	0.05
ZnO	0.13	0.09	0.05	0.13	0.05	0.01	0.06	0.09	0.03
Total	98.77	98.39	97.99	95.66	96.97	96.62	96.51	96.49	98.98
Numbers of ions on the basis of 3 cations for spinels, and 2 cations for ilmenite									
Si	0.003	0.003	0.003	0.001	0.005	0.003	0.003	0.011	0.000
Al	0.279	0.269	0.279	0.148	0.109	0.072	0.104	0.071	0.002
V	0.009	0.009	0.010	0.018	0.014	0.006	0.023	0.017	0.005
Cr	1.625	1.627	1.598	0.514	0.023	0.003	0.055	0.086	0.002
Fe^{3+}	0.049	0.056	0.072	0.189	1.192	0.631	0.564	0.407	0.101
Ti	0.015	0.016	0.017	0.564	0.326	0.641	0.624	0.698	0.945
Mg	0.241	0.249	0.148	0.099	0.019	0.031	0.038	0.062	0.039
Ni	0.001	0.001	0.001	0.001	0.001	0.001	<0.001	0.001	0.000
Fe^{2+}	0.757	0.752	0.856	1.442	1.297	1.592	1.568	1.624	0.888
Mn	0.015	0.015	0.015	0.019	0.011	0.017	0.015	0.016	0.016
Ca	0.001	0.000	0.000	0.001	0.002	0.002	0.004	0.005	0.001
Zn	0.003	0.002	0.001	0.004	0.001	0.000	0.002	0.001	0.001
total	3.000	3.000	3.000	3.000	3.000	3.000	3.000	3.000	2.000
Cr#[b]	0.85	0.86	0.85	0.78	0.17	0.04	0.35	0.55	-
Chr	90	89	91	23	1	0	3	4	-
Mgt	3	3	4	8	63	30	28	18	-
Sp	5	5	3	2	0	0	1	1	-
Ulp	2	2	2	67	36	69	69	77	-
Ilm	-	-	-	-	-	-	-	-	95
Hem	-	-	-	-	-	-	-	-	5

[a]Chr = chromite, Mgt = magnetite, Sp = spinel, Ulp = ulvöspinel, Ilm = ilmenite, Hem = hematite. [b]Molar Cr# = [Cr/(Cr + Al)].

current classification system for Martian meteorites must evolve to accommodate the full complexity of Mars' geological history. This underscores the need for a dynamic and adaptable classification methodology, one that not only incorporates present understanding but also anticipates future advancements (Herd et al., 2024, 2025).

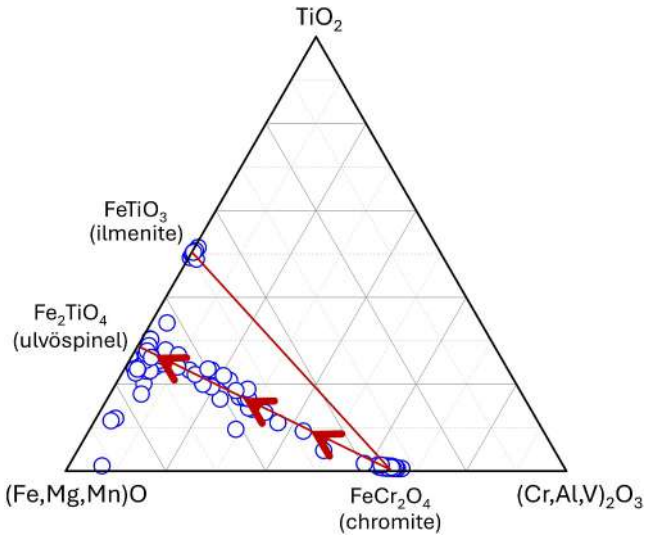

Figure 9. Ternary plot showing the composition of spinels in NWA 16788 after El Goresy et al. (1971) diagram. The red arrow illustrates the compositional evolution from chromite to the ulvöspinel end-member.

Thus, transitioning toward a terrestrial-like classification (Figures 16b–16f), instead of strictly adhering to the traditional scheme (e.g., poikilitic, Figure 16a), may offer a more effective framework—particularly for mafic and ultramafic plutonic-like rocks. A significant example is the poikilitic shergottite group, which exhibits a broad range of petrographic lithologies when classified using the modal proportions of olivine (Ol), orthopyroxene (Opx), and clinopyroxene (Cpx) in the ultramafic rock classification (Figure 16e). Such variability suggests a more complex petrological framework than traditionally implied by the term "poikilitic." Therefore, refining the current classification system may have important implications for the classification of Martian rocks returned by future Mars Sample Return missions (Herd et al., 2025; McCubbin et al., 2025; Udry et al., 2025), as well as for improving correlations between Martian meteorites and igneous rocks observed on Mars based on rover-collected data (e.g., Liu et al., 2022).

In light of these considerations, it is possible that some poikilitic (e.g., NWA 10169, Combs et al., 2019) and basaltic shergottites (e.g., NWA 480, Barrat et al., 2002) may be more appropriately grouped within the same taxonomic lithology, potentially analogous to the terrestrial gabbroic suite—a view also recently supported by Saper et al. (2025). Accordingly, we propose that NWA 16788 should be classified as an olivine microgabbroic rather than basaltic or poikilitic shergottite.

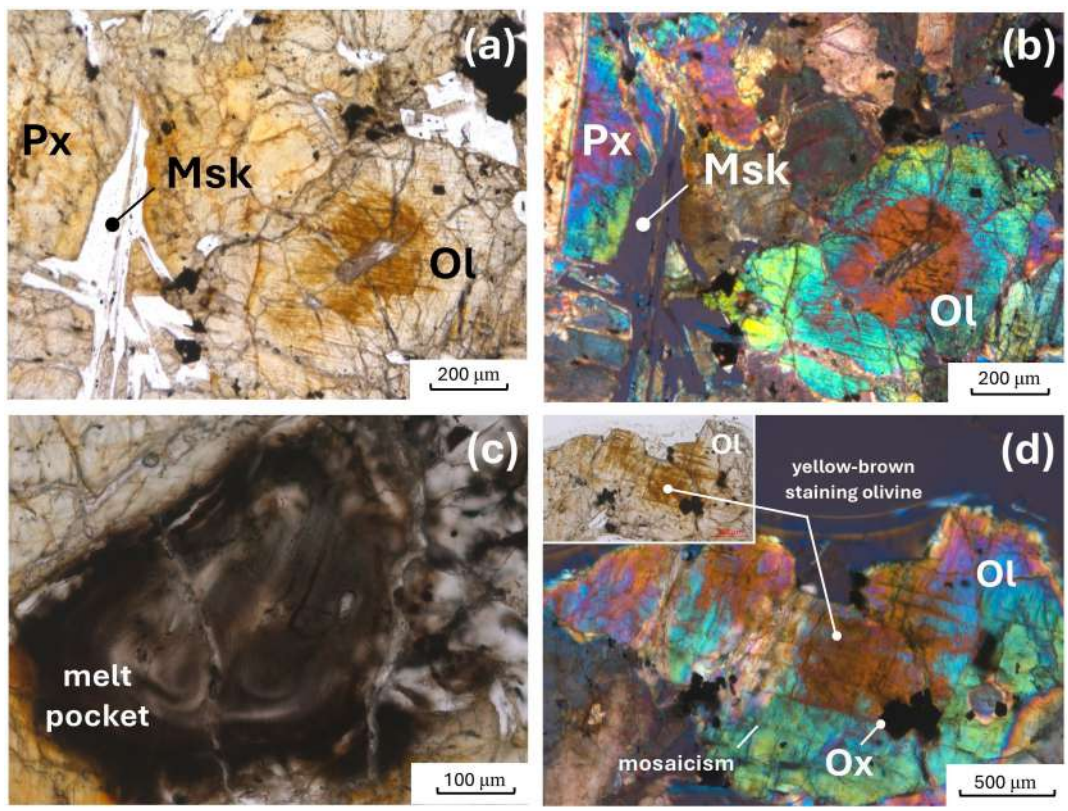

Figure 10. Optical thin-section microphotos displaying the shock-induced features in NWA 16788. (a) Transmitted plane-polarized light and crossed polars (b) microphotos of the high-shock portion mainly composed of maskelynite (Msk), pyroxene (Px), and olivine (Ol). (c) Shock-induced melt pocket in transmitted plane-polarized mode. (d) High-shocked yellow-brown staining olivine grain with mosaicism and oxide (Ox) inclusion in crossed polar mode.

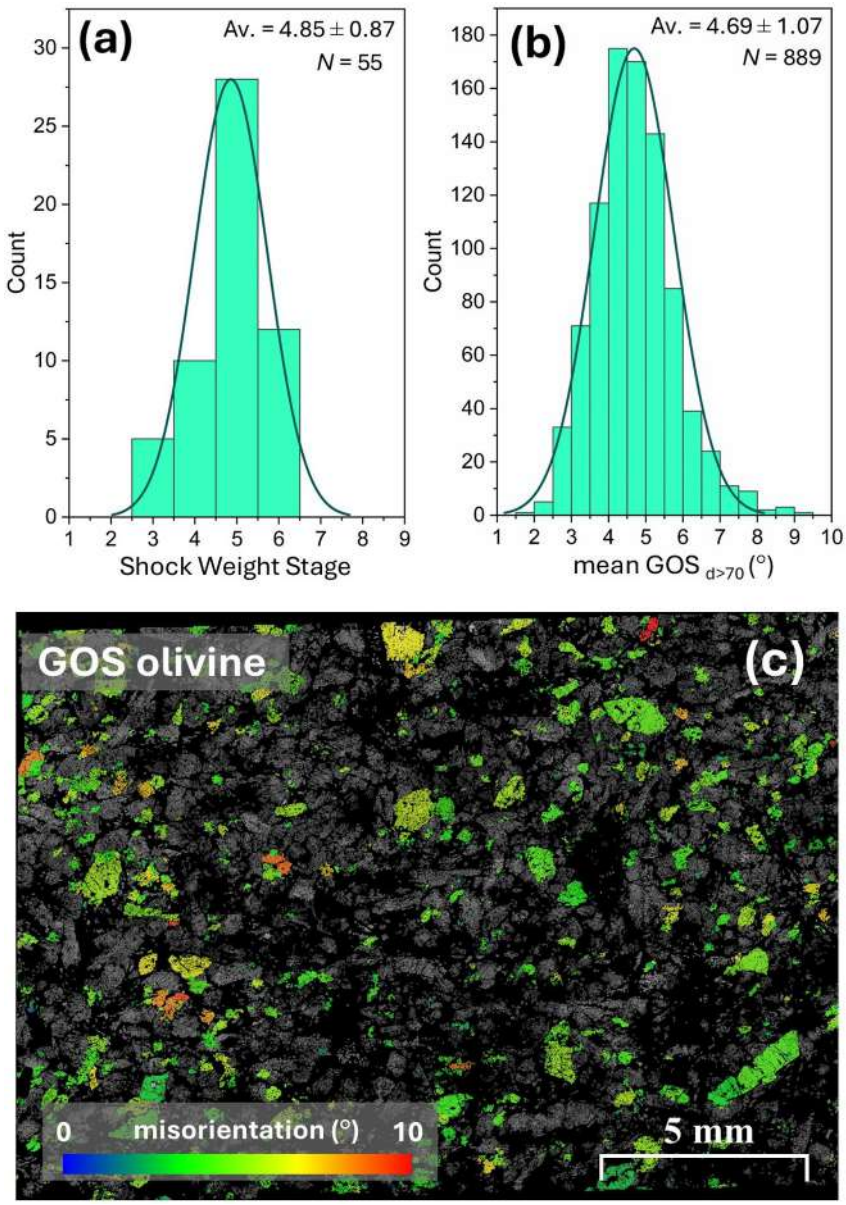

Figure 11. Shock stage in NWA 16788 estimated by different methods. (a) Shock weight stage of olivine grains (>70 μm in diameter) estimated by Jamsja and Ruzicka (2010) method. (b) Mean Grain Orientation Spread (GOS) for olivine grains >70 μm in equivalent diameter. (c) Large area map showing GOS deformation values for olivine grains overlapped with band contrast map.

Despite the taxonomic ambiguities discussed above, we found that NWA 16788 differs from poikilitic shergottites, which are characterized by a typically bimodal pyroxene composition, large pyroxene oikocrysts (>3 mm), and a low maskelynite abundance (<20 vol.%). Furthermore, its poikilitic texture, cumulate origin, high olivine content (15.3 vol.%), and millimeter grain-size also distinguish it from typical basaltic shergottites. Finally, the grain size in NWA 16788 (average ~0.7 mm) is smaller than in other gabbroic and olivine-gabbroic shergottites (typically ≥1 mm; e.g., NWA 13134 and NWA 13227; Saper et al., 2025; Benaroya et al., 2024), further supporting its classification as an olivine microgabbroic shergottite.

4.2. Shock Petrography

The presence of melt pockets, complete maskelynitization, and mosaicism in olivine grains (Figure 10) suggests significant shock metamorphism. The occurrence of yellow-brown staining observed in olivine, interpreted as

Table 4
Major, Minor, Trace Elements, Nd and Sr Isotopic Composition of NWA 16788 and Other Gabbroic and Olivine-Gabbroic Shergottites

Data	This study				Filiberto et al. (2018)	Saper et al. (2025)	Benaroya et al. (2024)	Wu et al. (2023)
Meteorite	NWA 16788				NWA 6963	NWA 13134	NWA 13227	NWA 13581
Petrography	Olivine microgabbroic				Gabbroic	Gabbroic	Olivine-Gabbroic	Olivine-Gabbroic
Geochemistry	Enriched				Enriched	Enriched	Enriched	Enriched
Major and minor elements								
Methods	EMPA		ICP-MS		EMPA	XRF	EMPA	ICP-OES
(wt%)		*1σ*		*2σ*				
SiO_2	48.21	*0.85*	-	-	49.23	48.60	-	-
TiO_2	0.41	*0.25*	0.74	*0.05*	0.77	1.01	0.57	0.61
Al_2O_3	5.51	*0.33*	5.63	*0.67*	3.13	6.09	4.55	4.86
Cr_2O_3	0.50	*0.37*	0.56	*0.03*	0.24	0.20	0.65	0.68
FeO	20.45	*2.87*	19.55	*1.27*	21.26	22.3[a]	18.94	23.8
MnO	0.53	*0.06*	0.50	*0.03*	0.60	0.53	0.47	0.51
MgO	15.58	*1.78*	14.12	*0.85*	11.41	9.49	15.39	17.6
CaO	6.27	*1.45*	-	-	10.48	9.36	6.47	5.68
Na_2O	1.03	*0.08*	1.04	*0.06*	0.77	1.29	0.79	0.94
K_2O	0.08	*0.02*	-	-	0.10	0.23	0.10	0.11
P_2O_5	0.62	*0.02*	-	-	0.83	1.03	0.54	-
Mg#[b]	57.6	*8.29*	56.3	*4.2*	48.9	45.7	59.2	56.9
Trace elements								
ppm		*2σ*						
Li	6.36	*0.37*			4.34	-	-	3.44
Be	0.292	*0.007*			-	-	-	-
Sc	36.50	*2.32*			51.1	14.8	58.73	28.9
V	211.5	*7.7*			269	252	109.54	206
Cr	3802.4	*196.2*			1,491	-	-	4,656
Co	51.5	*2.1*			-	34.4	53.36	58.6
Ni	179.4	*7.5*			101	68	191.26	224
Cu	14.17	*25.95*			16.3	16.3	12.07	9.96
Zn	80.6	*9.5*			106	86.1	72.04	71.0
Ga	11.37	*0.75*			-	15.2	18.44	10.3
Rb	5.18	*0.33*			6.10	7.50	2.82	4.05
Sr	65.9	*2.9*			62.5	52.2	44.23	35.9
Y	15.00	*0.92*			18.2	17.1	16.55	10.8
Zr	55.3	*2.8*			64.5	67.6	40.71	43.6
Nb	3.71	*0.09*			8.94	2.49	3.61	8.72
Mo	0.082	*0.015*			0.82	0.08	0.16	6.49
Sn	0.24	*0.05*			-	0.46	0.15	0.304
Sb	0.07	*0.03*			-	-	-	0.012
Cs	0.343	*0.052*			0.43	0.51	-	0.256
Ba	115.3	*7.7*			88	63.0	115.74	18.3
La	2.25	*0.19*			2.59	2.84	2.60	1.48
Ce	5.48	*0.28*			6.22	6.73	5.70	3.49

Table 4
Continued

Data		This study	Filiberto et al. (2018)	Saper et al. (2025)	Benaroya et al. (2024)	Wu et al. (2023)
Pr	0.735	*0.053*	0.85	1.05	0.92	0.514
Nd	3.73	*0.34*	4.18	4.67	4.20	2.51
Sm	1.42	*0.08*	1.60	1.66	1.52	0.982
Eu	0.539	*0.033*	0.58	0.73	0.70	0.397
Gb	2.23	*0.15*	2.54	2.72	2.31	1.53
Tb	0.404	*0.02*	0.48	0.59	0.49	0.283
Dy	2.81	*0.17*	3.25	3.72	2.99	2.00
Ho	0.575	*0.03*	0.68	0.82	0.63	0.413
Er	1.62	*0.08*	1.95	2.31	1.82	1.28
Tm	0.228	*0.022*	0.28	0.34	0.33	0.173
Yb	1.45	*0.06*	1.77	1.85	1.52	1.07
Lu	0.204	*0.012*	0.25	0.32	0.26	0.156
Hf	1.61	*0.10*	1.93	2.22	1.25	4.36
Ta	0.193	*0.039*	0.57	0.13	0.27	4.65
W	0.359	*0.024*	0.61	-	0.49	-
Pb	0.460	*0.064*	0.87	0.83	0.48	0.024
Th	0.397	*0.023*	0.50	0.51	0.59	0.273
U	0.209	*0.010*	0.14	0.16	0.16	0.066
Nd and Sr isotopic composition[c]						
$^{87}Sr/^{86}Sr$	0.719444 ± 5		-	-	-	0.722771 ± 5
$^{143}Nd/^{144}Nd$	0.512282 ± 1		-	-	0.512337 ± 3	0.512312 ± 3
$\varepsilon^{143}Nd$	(6.94 ± 6		-	-	(5.85	(6.36

Note. Italics are referred to as error. [a]Expressed as Fe_2O_3. [b]Molar Mg# = [Mg/(Mg + Fe)]100. [c]The uncertainties correspond to the last significant figures and are reported at the 2σ level for the isotopic composition for NWA 16788.

shock-induced iron oxidation, further confirms a high shock stage (Dyar, 2003; Kurihara et al., 2008; McSween & Stöffler, 1980; Ostertag et al., 1984; Papike et al., 2009; Stöffler et al., 1986, 2018; Van de Moortèle et al., 2007). The entire conversion of plagioclase to maskelynite indicates shock pressures of at least 30 GPa (Stöffler et al., 1991), although recent experimental studies suggest that complete maskelynitization can occur at 17–22 GPa (Hu et al., 2023).

A recently developed approach for assessing shock metamorphism utilizes SEM-EBSD to quantitatively characterize olivine deformation resulting from impact events (Anim & Ruzicka, 2024; Ruzicka & Hugo, 2018). This technique has demonstrated utility in estimating shock grades in meteoritic materials. In case of NWA 16788, olivine grains exhibited a mean $GOS_{d>70}$ value of 4.69 ± 1.07 and a "weighted shock stage (WSS)" of 4.85 ± 0.87, in agreement with a linear trend observed in shocked ordinary chondrites (Figure 17a). The unimodal $GOS_{d>70}$ distribution suggests a single-collision event, plausibly the same event that led to its ejection into interplanetary space.

4.3. Weathering Grade

The preservation of pyrrhotite grains indicates minimal terrestrial weathering (TW) for NWA 16788 (Figure 4), consistent with a W1 rating on the Wlotzka scale, where W0 represents a fresh fall and W6 indicates extensive alteration (Wlotzka, 1993).

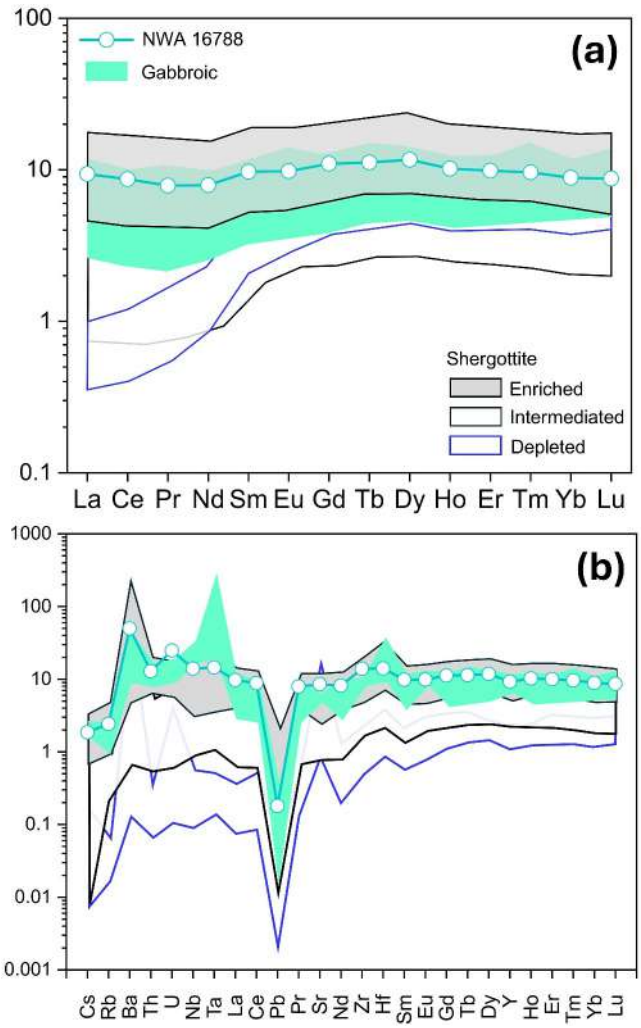

Figure 12. Bulk trace element composition of NWA 16788 compared with representative literature data. (a) Chondrite-normalized Rare Earth Element (REE) patterns and trace element patterns (b) for NWA 16788 (normalized to CI-chondrite from Lodders, 2003), compared with enriched, intermediate, and depleted shergottites (data are from Udry et al., 2020 and references therein), as well as gabbroic and olivine gabbroic shergottites (data are from Benaroya et al. (2024), Filiberto et al. (2018), Saper et al. (2025), Udry et al. (2017), and Wu et al. (2023)).

The enrichment of fluid-mobile elements, such as Ba and Sr, is used to assess TW in ordinary chondrites (OC) (e.g., Al-Kathiri et al., 2005), and a similar approach has been applied to Martian meteorites (e.g., Barrat et al., 2002; Filiberto et al., 2018; Howarth et al., 2018). However, because Martian meteorites are differentiated igneous rocks, enrichment in incompatible elements (e.g., Ta and Ba) may also reflect petrological processes, including partial melting of distinct sources. To better assess the effects of weathering, we adopt the Ta/Yb ratio as an index of Martian shergottite enrichment (minimally influenced by TW) and the Ba/Yb ratio as a marker for TW (highly susceptible to TW). Figure 17b shows a continuous increase in the Ta/Yb and Ba/Yb ratios from depleted to enriched shergottites, reflecting distinct geochemical reservoirs. This is supported by the enriched trend observed in Tissint, Zagami, and Shergotty, the only shergottites observed to have fallen. We found that some samples, such as the highly weathered DaG 467, show minimal variation in Ta/Yb [avg. = 0.013 ± 0.001] but significantly high and variable Ba/Yb [avg. = 93.06 ± 61.29], which can be attributed to TW. While NWA 16788 shows slight Ba/Yb shifting (Figure 17b), it does not deviate significantly from the enriched shergottite trend, suggesting a moderate chemical TW. These geochemical interpretations are further supported by reflectance spectroscopy data, which reveal no significant absorption related to secondary hydrated phases (e.g., clay minerals) or carbonates, except for a weak feature around 1.9 μm observed only on slab data. Potential charge transfers due to oxidation (e.g., Fe^{2+}/Fe^{3+}) in the visible and beginning of NIR are also negligible.

4.4. Pyroxene Relationship With Other Shergottites and Lunar Samples: Thermal History

Previous studies have pointed out that a small group of shergottites (EETA 79001A, EETA 79001B, and QUE 94201) share a distinctive pyroxene zoning pattern, starting with an Mg-rich pigeonite core, followed by augite mantle crystallization, and finally rimmed by Fe-rich pigeonite (McSween et al., 1996; Mikouchi et al., 1998, 1999). A similar sequence was first observed in the pyroxene crystals of Apollo 15 basalts (Bence & Papike, 1972) and was subsequently experimentally reproduced in a synthetic analog of Apollo 15 basalt 15597 (Grove & Bence, 1977). The growing number of Martian meteorite samples has shown that other types of shergottite (e.g., LAR 06319, NWA 5298, NWA 13227), including the NWA 16788 analyzed in this study, as well as the lunar meteorite (NEA 003-A), exhibit the same pyroxene chemical evolution (Benaroya et al., 2024; Haloda et al., 2009; Hui et al., 2011; Sarbadhikari et al., 2009).

As shown in Figure 18, various basalts, ranging from olivine-free basaltic shergottites to olivine-gabbroic shergottites and olivine-bearing lunar basalts, display similar pyroxene chemical evolution. The interpretation of this zoning trend has been a topic of debate in the past (Bence & Papike, 1972; Bence et al., 1971; Boyd & Smith, 1971; Dowty et al., 1974; Grove & Bence, 1977; Hollister et al., 1971). However, there is now a broad consensus that Mg-rich pigeonite cores crystallize first, increasing calcium levels in the residual melt. This promotes the formation of augite mantles in a non-equilibrium process, driven by the suppression of plagioclase crystallization (e.g., Barrat et al., 2002; Grove & Raudsepp, 1978; Hui et al., 2011; McSween et al., 1996; Mikouchi et al., 1998; Mikouchi et al., 1999; Peslier et al., 2010). As the magma cools and crystallization progresses, the increasing saturation of Ca and Al in the residual melt leads to late-stage plagioclase crystallization followed by the formation of typically Fe-rich pigeonite rims. Several authors suggest that the evolution of pyroxene zoning is strongly influenced by the magma's restricted cooling rate, which plays a critical role in controlling the crystallization sequence and zoning patterns (Grove & Bence, 1977; Grove & Raudsepp, 1978; McSween et al., 1996 and references therein, Mikouchi et al., 1998; Mikouchi et al., 1999). In particular, the formation of augite mantles appears to require

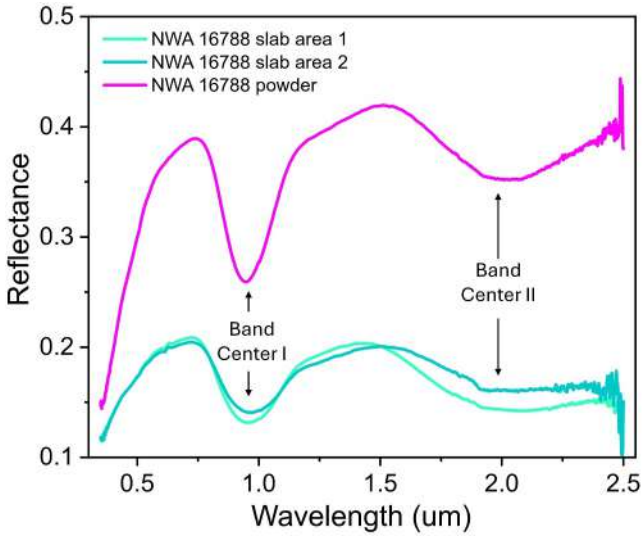

Figure 13. Reflectance spectra from the powder and slab area of NWA 16788.

relatively fast cooling (150–60°C/h) to suppress plagioclase nucleation, allowing Ca to partition into the pyroxene (Grove & Bence, 1977; Peslier et al., 2010). Additionally, controlled petrological experiments have replicated similar pyroxene zoning patterns starting with a synthetic analog of Apollo 15 basalt 15597 under cooling rates less than 0.5°C/hour (Barrat et al., 2002 and references therein). Collectively, these findings, including the case of NWA 16788, suggest that such thermal histories may have been more prevalent in Martian magmatic systems than previously recognized.

4.5. Differentiation and Crystallization Sequence

Primary magma refers to magma formed by the partial melting of a mantle source whose composition has not been subsequently modified by differentiation processes (e.g., fractional crystallization). Thus, identifying whether the composition of the analyzed igneous sample represents primary magma is fundamental in petrology as it provides insight into differentiation processes. Since olivine and pyroxene are among the first minerals to crystallize, primary magmas must be in equilibrium with these phases. It has been shown that the distribution of Fe and Mg between olivine and the coexisting melts is governed by the partitioning coefficient (K), defined by the relation $K_{D\mathrm{Ol/melt}}^{\mathrm{Fe/Mg}}$ (1) (Filiberto & Dasgupta, 2011 and references therein). This coefficient is an effective parameter for determining whether the melt composition represents a true primary magma. Assuming the bulk composition as a melt and considering the most magnesian olivine, the calculated partition coefficient $K_{D\mathrm{Ol/melt}}^{\mathrm{Fe/Mg}}$ for NWA 16788 is 0.51, which significantly deviates from the equilibrium $K_{D\mathrm{Ol/melt}}^{\mathrm{Fe/Mg}}$ value of 0.35 inferred in Martian basalt experiments, surface rocks, and meteorites (Filiberto & Dasgupta, 2011). This discrepancy suggests that NWA 16788 was not in chemical equilibrium with its parent magma. This is consistent with petrographic observations from gabbroic shergottites, many of which are thought to contain cumulate crystals (e.g., Udry et al., 2020).

$$K_{D\mathrm{Ol/melt}}^{\mathrm{Fe/Mg}} = \left(\mathrm{Fe}^{2+}/\mathrm{Mg}\right)_{\mathrm{olivine}}/\left(\mathrm{Fe}^{2+}/\mathrm{Mg}\right)_{\mathrm{melt}} \quad (1)$$

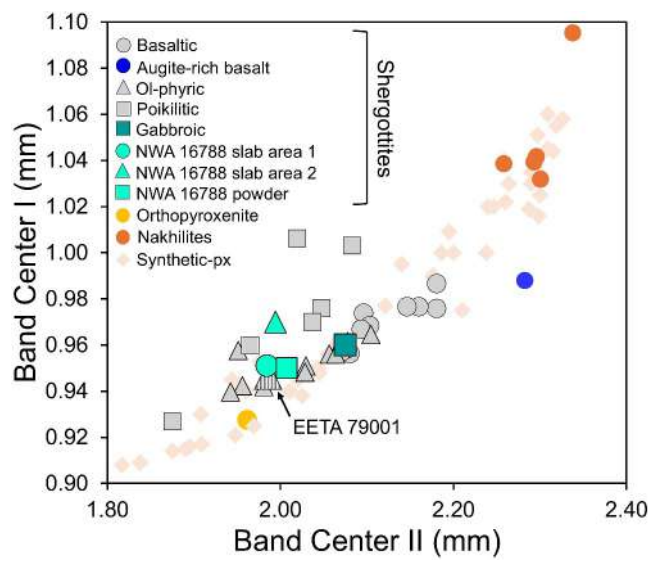

Figure 14. Band Center II versus Band Center I, showing the variation of spectral properties of NWA 16788 relative to synthetic pyroxene from Klima et al. (2007, 2008, 2011), as calculated by Burbine et al. (2018), and compared with data from Madon et al. (2021, modified after their Figure 12a) and Filiberto et al. (2018).

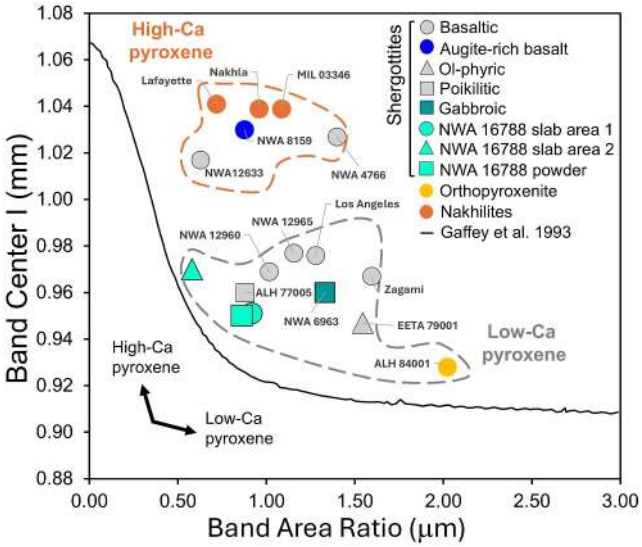

Figure 15. Band Center I versus Band Area Ratio. This relationship shows how the data from Martian meteorites (NWA 16788 and other data related to spectra of powders from Filberto et al., 2018; Mandon et al., 2021) are plotted on the right side with respect to the line related to the ol-opx trend. Two domains can be highlighted, mainly related to the composition of the host-dominating pyroxene (low-Ca pyroxene and high-Ca pyroxene).

$$K_{D\,\mathrm{Ol/low(\,Ca(\,Px}}^{\mathrm{Mg/Fe}} = \left(\mathrm{Mg/Fe^{2+}}\right)_{\mathrm{olivine}} / \left(\mathrm{Mg/Fe^{2+}}\right)_{\mathrm{low(\,Ca(\,Px}} \quad (2)$$

$$(\mathrm{Mg,Fe,Ca})_2\mathrm{Sio}_{4(\mathrm{Chadacryst})} + \mathrm{Liquid} \Leftrightarrow (\mathrm{Mg,Fe,Ca})(\mathrm{Mg,Fe})\,[\mathrm{Si_2O_6}]_{(\mathrm{oikocryst})} \quad (3)$$

The texture and mineral chemistry of NWA 16788 provide key insights into its crystallization history. Large olivine and pyroxene crystals, frequently enclosing chromite inclusions, are euhedral to subhedral, indicating they were among the earliest phases to crystallize. We determined an Mg-Fe partition coefficient ($K_{D\,\mathrm{Ol/low(\,Ca(\,Px}}^{\mathrm{Mg/Fe}}$) of 0.89 between olivine and low-Ca pyroxene in NWA 16788 (Equation 2). Typically, a $K_{D\,\mathrm{Ol/low(\,Ca(\,Px}}^{\mathrm{Mg/Fe}}$ value of 1.2 indicates that Mg is slightly more compatible with olivine during equilibrium crystallization in shergottite basaltic magmas (Longhi & Pan, 1989). Thus, the lowest observed value of 0.89 suggests that the pyroxene cores likely crystallized after the initial olivine, similar to what was observed in NWA 6234 (Gross et al., 2013), as well as LAR 06319, Tissint, and many other olivine-phyric, and olivine-gabbroic shergottites (Benaroya et al., 2024; Liu et al., 2016; Peslier et al., 2010; Sarbadhikari et al., 2009).

During a competitive nucleation and crystals' growth, a chemical interaction between olivine and pyroxene may have taken place, where enclosed olivine chadacrysts were partially reabsorbed by pigeonitic pyroxene oikocrysts in a poikilitic texture. These processes, potentially driven by the reaction (3), could explain the observed Ca depletion of olivine chadacrysts and the observed reabsorption circular edge. As crystallization continued, the pyroxene composition evolved during the crystallization sequence from Mg-rich to Ca-rich, continuing until the onset of plagioclase crystallization, while olivine became increasingly Fe-rich. The formation of Fe-rich pigeonite rims is typically attributed to the crystallization of plagioclase, which trapped Ca from the melt, leading to a relative enrichment of Fe in the residual liquid (e.g., McSween et al., 1996; Peslier et al., 2010). Moreover, exsolution lamellae in some Fe-rich pigeonite rims suggest a complex thermal history for NWA 16788, likely involving crystallization in non-equilibrium conditions, as previously proposed for EETA 79001 shergottite (Mikouchi et al., 1999). Crystallization progresses with lath-like phosphate crystals, prompted by the increased phosphorous concentration in the residual magma. The final stages of crystallization are defined by anhedral aggregates of merrillite, apatite, spinel, ilmenite, and pyrrhotite formed from the residual melt confined within interstitial cavities. The crystallization sequence proposed for NWA 16788 is illustrated in Figure 19. A similar sequence has been suggested for other shergottites exhibiting comparable petrography and pyroxene zoning, such as NWA 13227 (Benaroya et al., 2024).

4.6. Igneous Petrogenesis

The $^{143}Nd/^{144}Nd$ and $^{87}Sr/^{86}Sr$ ratios are particularly significant in Martian meteorites as differences in isotopic composition reflect distinct magmatic reservoirs (e.g., Borg et al., 2002; Borg & Draper, 2003; Day et al., 2018). The high $^{87}Sr/^{86}Sr$ ratio (0.719444) and low $\varepsilon^{143}Nd$ value ((6.94) of NWA 16788 are consistent with those of other enriched shergottites (Figure 20a). These characteristics indicate derivation from an ancient mantle reservoir that has retained an enriched composition over the long–term (Blichert-Toft et al., 1999; Borg & Draper, 2003; Borg et al., 1997, 2003, 2016; Brandon et al., 2000; Harper et al., 1995). This enrichment signature is also well expressed in the high concentrations of incompatible elements in NWA 16788, such as Th/Yb and Ta/Yb (Figure 20b), which likely result from partial melting of a mantle source enriched in incompatible trace elements (e.g., Day et al., 2024). In this regard, it was previously proposed that the diversity of geochemical reservoirs in shergottites, from depleted to enriched, was correlated with progressively increasing oxygen fugacity (Herd, 2003; Herd et al., 2002). This implied that enriched shergottites formed under more oxidizing conditions while depleted ones formed under more reducing conditions. However, recent studies indicate that this correlation is less pronounced than initially recognized (e.g., Benaroya et al., 2024; Combs et al., 2019; Nicklas et al., 2021; Wu et al., 2023).

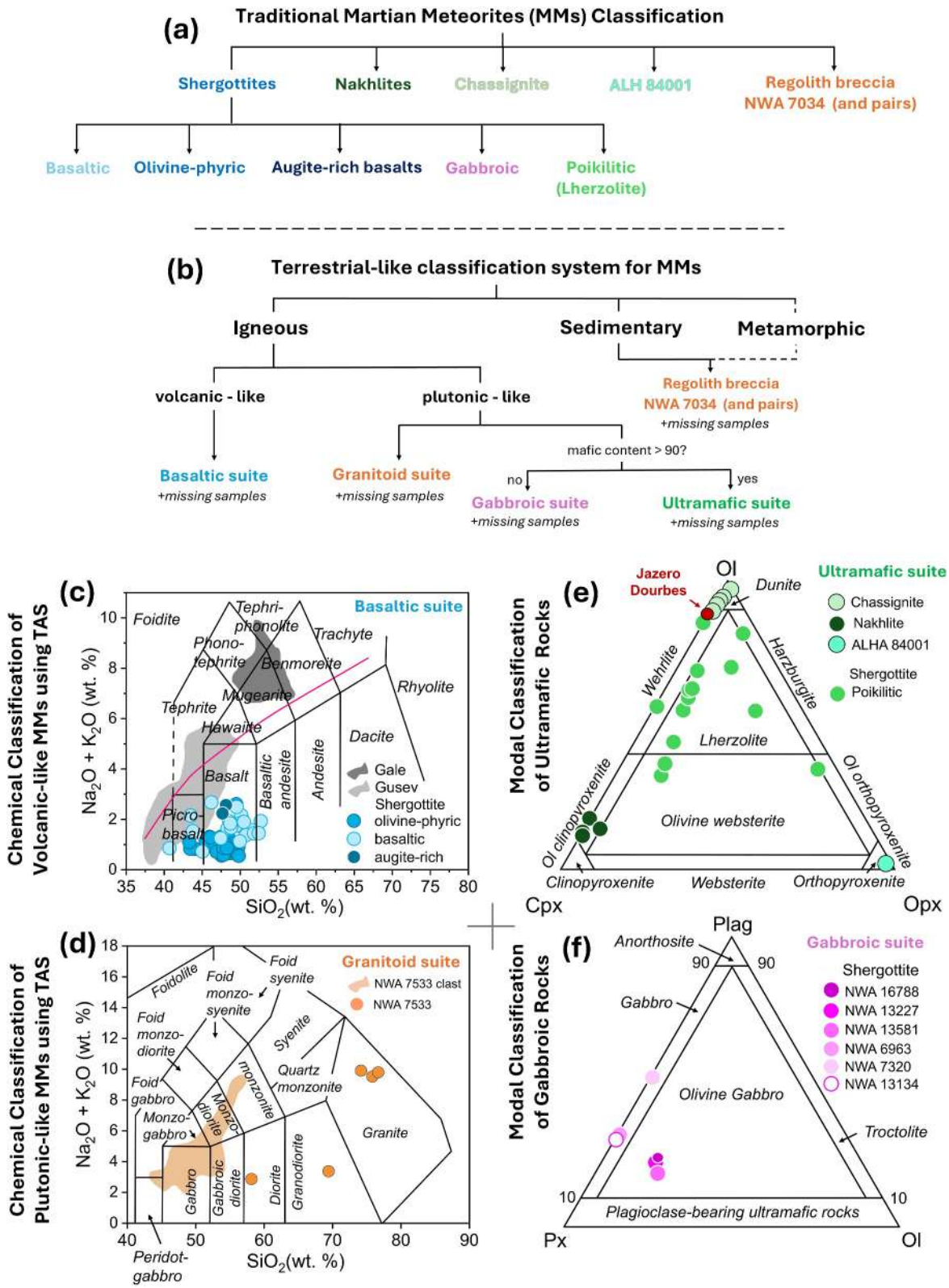

Figure 16.

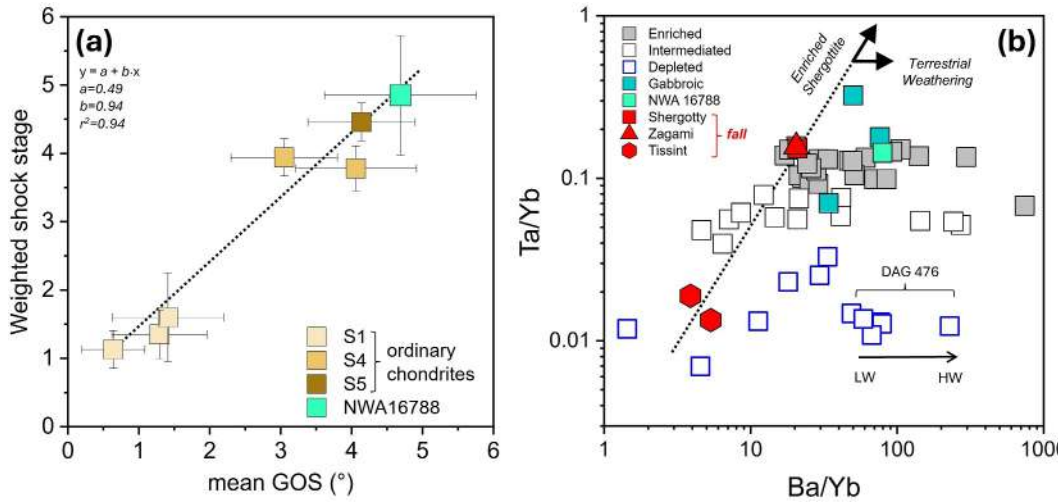

Figure 17. Shock-stage olivine deformation and terrestrial weathering in NWA 16788 compared with literature data. (a) Mean $GOS_{d>70}$ (°) value versus weighted shock stage diagram of olivine grains in NWA 16788, compared with literature data for olivine in ordinary chondrites (OC) where mean GOS major to 50 μm grain-sized (Ruzicka & Hugo, 2018). (b) Barium/Yb (terrestrial weathering index) versus Ta/Yb (enriched shergottite index) diagram for NWA 16788 compared with literature data (shergottite data are from Udry et al. (2020) and reference therein; gabbroic and olivine-gabbroic shergottites data are from Benaroya et al., 2024; Saper et al., 2025; Wu et al., 2023). The black arrow below DaG 476 data shows the terrestrial weathering evolution from low grade (LW) to high grade (HW).

Oxygen fugacity estimates based on Ol-Opx-Spn equilibria (Benaroya, 2023; Sack & Ghiorso, 1989, 1991a, 1991b, 1994a, 1994b, 1994c) suggest that NWA 16788 began crystallizing under reduced conditions at a subsolidus equilibration temperature of 1,156 ± 110°C and an fO_2 of approximately QFM–3.0 ± 0.2. This early-stage fO_2 is consistent with recent estimates for other enriched olivine-gabbroic shergottites, such as NWA 13581 and NWA 13227 (Benaroya et al., 2024; Wu et al., 2023), further supporting the conclusion that oxygen fugacity in shergottites is likely decoupled from their geochemical source (Nicklas et al., 2021). In contrast, oxygen fugacity derived from Fe-Ti oxide mineral equilibria suggests that late-stage crystallization of NWA 16788 occurred under more oxidizing conditions, reaching near the QFM buffer ((0.1 ± 0.3) at a temperature of 958 ± 119°C. This shift implies an increase in fO_2 of approximately three log units during magma crystallization relative to early-stage conditions near the iron–wüstite (IW) buffer (Figure 20c). Several processes may account for this progressive oxidation, including auto-oxidation during magma crystallization (Wu et al., 2023), volatile degassing (e.g., sulfur, Nicklas et al., 2021), and interaction with oxidized materials (Herd et al., 2002). Since auto-oxidation alone is thought to raise fO_2 by up to ~1 log unit (Castle & Herd, 2017; Combs et al., 2019), the higher increase observed in NWA 16788 likely reflects the combined effects of multiple oxidizing mechanisms.

Figure 16. Panoramic of Martian meteorites classification scheme and terms. (a) Traditional Martian meteorites classification scheme. (b) Simplified terrestrial-like classification scheme for Martian meteorites. Given the uncertain geological context of Martian meteorites—specifically, whether they originate from volcanic or plutonic settings—we adopt a simplified terrestrial-like classification scheme using the terms "volcanic-like" and "plutonic-like" to enable comparison between Martian meteorites and terrestrial igneous rocks. (c) Total Alkali-Silica (TAS) chemical classification of terrestrial rocks applied to volcanic-like shergottite meteorites. Shergottites literature data are from Udry et al. (2020) and Herd et al. (2017) for augite-rich shergottite, and Gale and Gusev compositional fields from McSween (2015). (d) Total Alkali-Silica classification for plutonic-like rocks applied to Martian meteorites according to Malarewicz et al. (2025). (e) Modal classification of ultramafic rocks by using the proportion of olivine (Ol), orthopyroxene (Opx), and clinopyroxene (Cpx) applied to Martian meteorites following the scheme proposed by Liu et al. (2022) and data from reference therein. The orthopyroxene ALH 84001 data are from Lapen et al. (2010). (f) Simplified modal classification of gabbroic rocks using the proportion of Ol, Cpx, and Plagioclase (Plag, or maskelynite). Literature data are from Udry et al. (2017), Filiberto et al. (2018), Wu et al. (2023), Benaroya et al. (2024), and Saper et al. (2025).

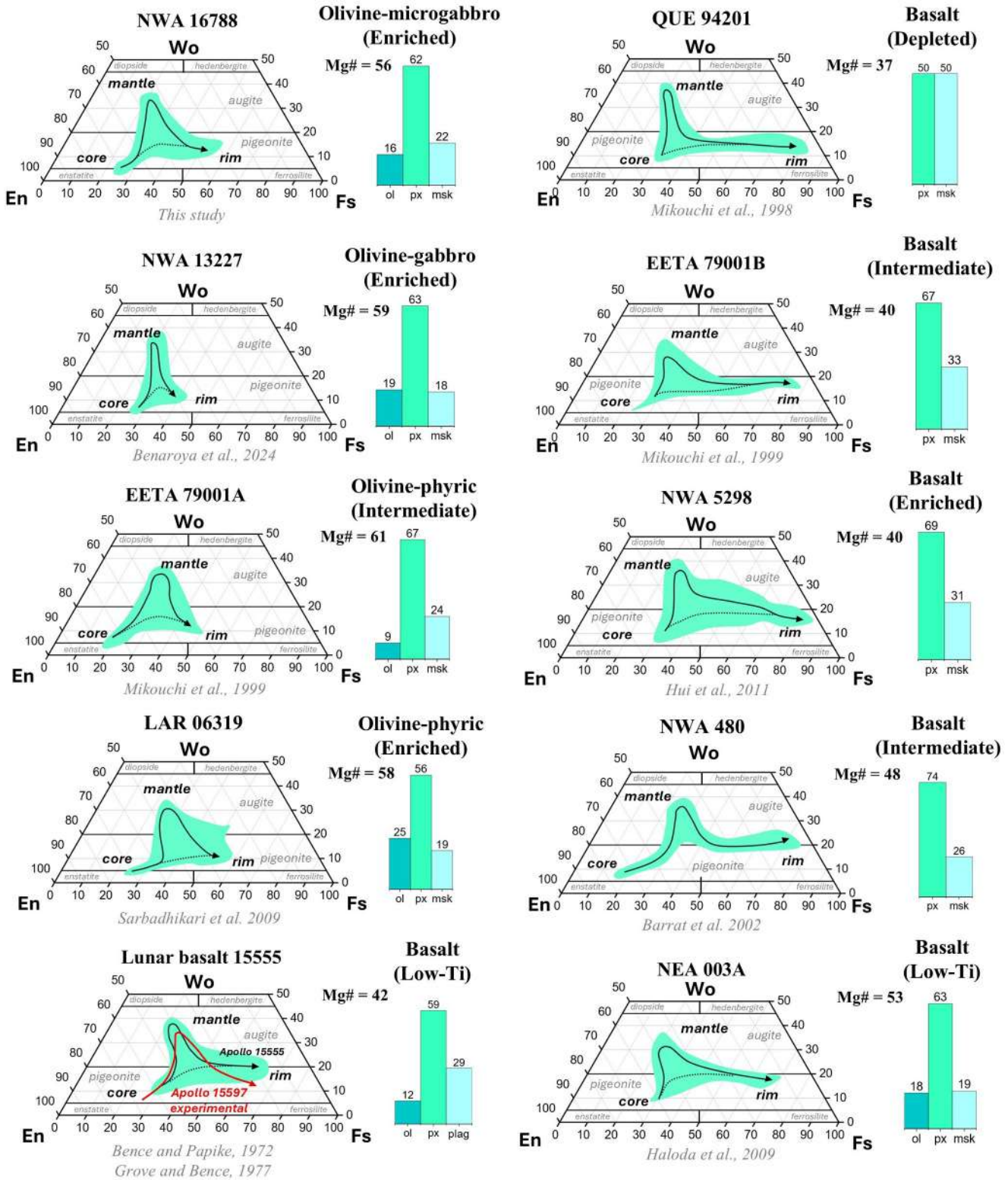

Figure 18. Quadrilateral pyroxene compositions of selected Martian shergottites, lunar meteorite NEA 003A, and Apollo sample 15555 showed similar pyroxene zoning patterns. The modal mineralogy is expressed as percentage abundance.

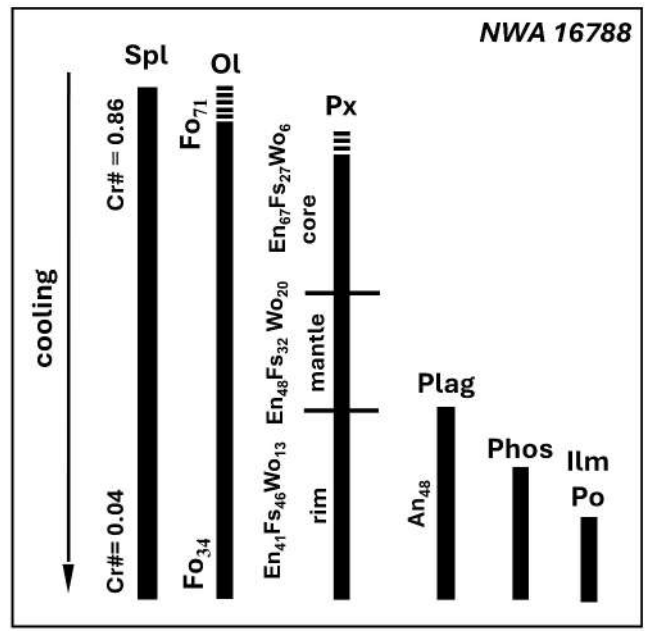

Figure 19. Crystallization sequence of NWA 16788 inferred from textural relationships and mineral chemical composition. Spinel (Spl), Olivine (Ol), Pyroxene (Px), Plagioclase (Plag), Phosphates (Phos), Ilmenite (Ilm), Pyrrhotite (Po).

4.7. Reflectance Spectroscopy and Comparison With Other Martian Meteorites

Visible and near-infrared reflectance spectroscopy reveals that the spectral features of NWA 16788 are primarily governed by the Mg-rich pigeonite core, with minimal contribution from the augitic mantle and Fe-rich pigeonite rim. The high absorption features of Mg-rich pigeonite in the VNIR reflectance spectrum, along with its greater abundance in comparison to other zoning domains, likely account for this observation. This spectral signature is consistent with previous observations in eucritic meteorites, where the host pigeonite controls the reflectance properties, despite the presence of exsolved augitic lamellae (Carli et al., 2022).

Considering the spectral framework established by Mandon et al. (2021), NWA 16788 falls within the textural and compositional range that spans both olivine-phyric and poikilitic shergottites (Figure 14). Notably, it shows close spectral parameters to EETA 79001, which exhibits a similar distinctive pyroxene evolution as illustrated in Figures 14 and 18. This similarity highlights the potential of VNIR spectra in distinguishing Martian meteorite groups and constraining their primary petrology. Other important parameters have been represented by the analysis of BC1 and BAR (Figure 15), which reveals two major spectral trends among Martian pyroxenes: one associated with high-Ca pyroxene composition, and another dominated by low-Ca pyroxene, where NWA 16788 plots.

Reflectance measurements in NWA 16788 from an olivine-enriched region (slab area 2) show a noticeable shift in band center positions (Figure 15), consistent with trends described by Cloutis et al. (1986). Thus, olivine abundance can influence VNIR spectral features, suggesting that the sampled area within an olivine micro-gabbroic texture may affect the resulting spectra (Figures 13–15). However, due to its low abundance in NWA 16788 (~15%), olivine contributes only modestly to the overall spectral signal. This highlights the importance of integrating petrological analyses with spectral data—particularly when interpreting in situ measurements or remote sensing observations of the Martian surface.

Overall, the marked correlation between the VNIR spectral features of NWA 16788 and those of well-characterized pigeonite-bearing Martian meteorites supports the efficacy of VNIR spectrometry as a tool for resolving the petrographic diversity of Mars (Mandon et al., 2021). Instruments such as SuperCam onboard the

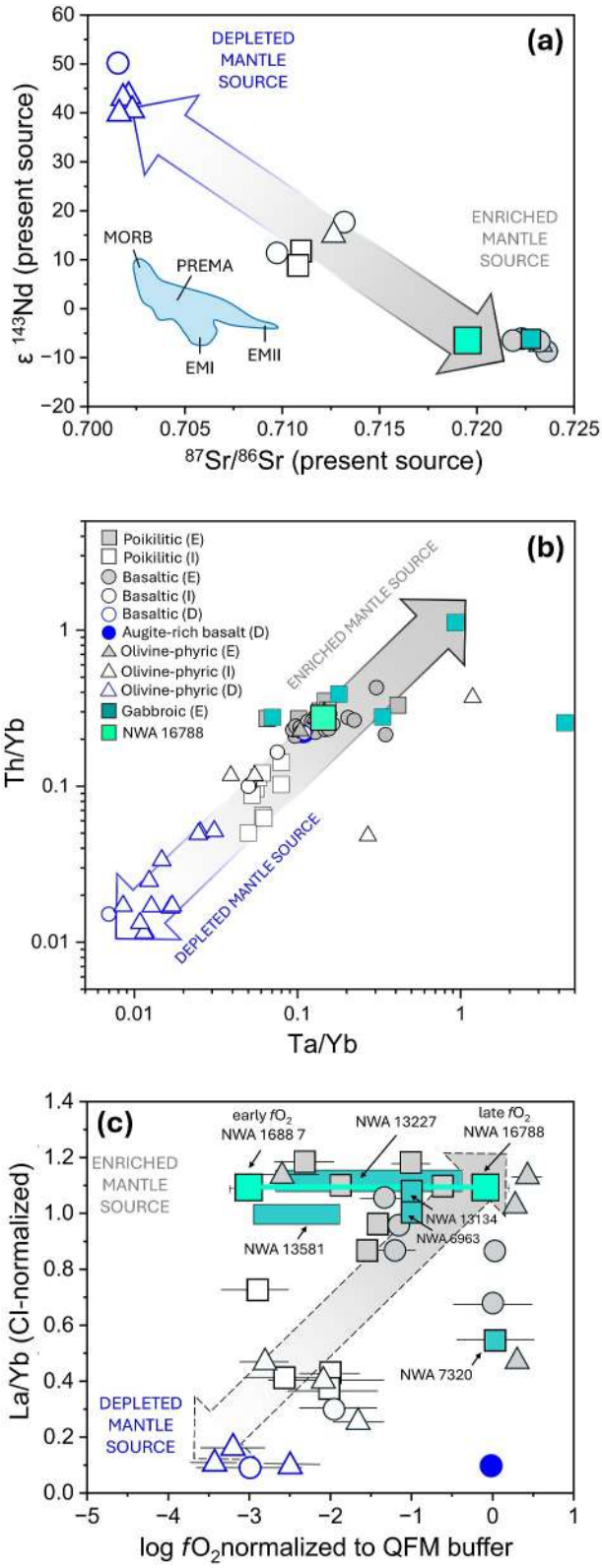

Figure 20.

Mars 2020 rover (e.g., Mandon et al., 2023; Royer et al., 2025; Udry et al., 2023) and the upcoming MicrOmega onboard the ExoMars rover (Bibring et al., 2017) can therefore contribute significantly to our understanding of Martian petrogenesis and geological diversity.

5. Conclusions

We conducted a comprehensive petrographic and geochemical investigation of NWA 16788, a newly identified olivine microgabbroic shergottite. This specimen is characterized by a cumulated texture dominated by millimeter-sized pyroxene grains, maskelynite, and olivine, with mineralogical and textural features common to both poikilitic and gabbroic shergottites. Accessory phases include chromite, ulvöspinel, ilmenite, apatite, merrillite, and pyrrhotite. Pyroxene crystals exhibit distinctive chemical zoning, starting with an Mg-rich pigeonite core, surrounded by an augite mantle, and rimmed by Fe-rich pigeonite. These distinct zoning patterns link NWA 16788 to a specific group of Martian meteorites and lunar samples that share a unique cooling history, suggesting that similar samples may be more widespread in Martian igneous rocks than previously recognized.

The average misorientation within olivine grains, measured using advanced electron backscatter diffraction techniques, reveals an unimodal distribution with a mean value of ~4.6°. These measurements correlate with petrographic observations, indicating a weighted shock stage of ~4.9, thus highlighting the potential of EBSD in characterizing the shock grade of Martian meteorites. Additionally, the geochemical diagram of Ta/Yb versus Ba/Yb indicates that NWA 16788 experienced moderate terrestrial weathering, implying that the sample has preserved most of its original geochemical signatures. Isotopic analyses of Nd and Sr reveal a high $^{87}Sr/^{86}Sr$ ratio (0.719444) and a low $\varepsilon^{143}Nd$ value ((6.94), indicating an origin from an enriched Martian mantle source. The calculated $K_{D_{Ol/melt}}^{Fe/Mg}$ partition coefficient of 0.51 suggests that NWA 16788 was not in chemical equilibrium with its parental magma, supporting a cumulate origin.

Oxygen fugacity estimates for NWA 16788 indicate crystallization under initially reduced conditions (fO_2 ~ QFM–3), similar to other enriched olivine-gabbroic shergottites. However, later-stage mineral equilibria reveal a significant increase in fO_2, reaching near the QFM buffer. This ~3 log unit rise suggests progressive oxidation during crystallization, likely driven by a combination of different processes, including auto-oxidation, volatile degassing, and possibly interaction with oxidized materials.

We found that the VNIR spectral features of NWA 16788 are primarily controlled by its Mg-rich pigeonite cores, with minor contributions from the augitic and Fe-rich rims. Its spectral parameters align with those low-Ca pyroxene Martian meteorites, such as EETA 79001, which also exhibit similar pyroxene zoning—highlighting the potential of VNIR spectrometry for mineralogical and petrographic discrimination. Additionally, we observed that olivine abundance can influence band parameters (e.g., Band Center I), suggesting that the specific area sampled within an olivine microgabbroic texture may affect the resulting spectra. This underscores the importance of integrating spectral data with petrological context and emphasize the potential of VNIR spectrometry—such as that employed by SuperCam and MicrOmega—for distinguishing Martian lithologies and unraveling the Mars's magmatic evolution.

Finally, new considerations for the refinements to the classification scheme of Martian meteorites are presented, aiming to reduce taxonomic ambiguity and improve alignment between Martian meteorites and Martian igneous rocks, based on data collected by Mars rovers.

Figure 20. Geochemical diagram comparison among different groups of Martian meteorites and NWA 16788. (a) Variation of $\varepsilon^{143}Nd$ versus $^{87}Sr/^{86}Sr$ isotopic composition referred to present-day shergottite sources. Data for poikilitic, olivine-phyric, and basaltic shergottites are from Symes et al. (2008) and reference therein, and olivine-gabbroic shergottite from Wu et al. (2023). Data for Earth isotopic composition are from Bezard et al. (2016) and reference therein. MORB = Mid-Ocean Ridge Basalts; PREMA = prevalent mantle; EMI/II = Enriched mantle I and II. (b) Variation of Th/Yb versus Ta/Yb illustrating the distinct geochemical groups within shergottites. Data for poikilitic, olivine-phyric, and basaltic shergottites are from Udry et al. (2020) and references therein. Data for the gabbroic and olivine-gabbroic shergottite are from Filiberto et al. (2018), Udry et al. (2017), Benaroya et al. (2024), Wu et al. (2023), and Saper et al. (2025). (c) Bulk-rock La/Yb ratios (CI-normalized, from McDonough & Sun, 1995) versus calculated oxygen fugacity in log units relative to the QFM buffer. Data for the poikilitic, olivine-phyric, and basaltic shergottites are from Combs et al. (2019) and references therein. Data for the gabbroic and olivine-gabbroic shergottites are from Udry et al. (2017), Benaroya et al. (2024), Wu et al. (2023), and Saper et al. (2025).

Data Availability Statement

The raw data used for characterizing NWA 16788 are available on Zenodo (Shehaj, 2025) with a Creative Commons Attribution 4.0 International license.

Acknowledgments
This research was financed by the Space It Up project funded by the Italian Space Agency, ASI, and the Ministry of University and Research, MUR, under contract n. 2024-5-E.0—CUP n. I53D24000060005. This paper and related research have been conducted during the Italian national inter-university PhD program in Space Science and Technology. The authors thank Dr. Tiziano Catelani and Dr. Laura Chiarantini for EBSD and SEM technical support, Dr. Chiara Maccelli for supporting ICP-MS and TIMS analysis, Dr. Eleonora Braschi and Dr. Andrea Orlando for the technical assistance during EMPA analysis. The authors also thank Dr. Luca Cableri for kindly providing the samples investigated in this study. We thank Sophie Benaroya and Yunhua Wu for helpful revisions, comments and suggestions, which have improved the quality of the manuscript. Open access publishing facilitated by Universita degli Studi di Firenze, as part of the Wiley - CRUI-CARE agreement.

References

Agee, C. B., Wilson, N. V., McCubbin, F. M., Ziegler, K., Polyak, V. J., Sharp, Z. D., et al. (2013). Unique meteorite from early Amazonian Mars: Water-rich basaltic breccia Northwest Africa 7034. *Science*, *339*(6121), 780–785. https://doi.org/10.1126/science.1228858

Al-Kathiri, A., Hofmann, B. A., Jull, A. J. T., & Gnos, E. (2005). Weathering of meteorites from Oman: Correlation of chemical and mineralogical weathering proxies with ^{14}C terrestrial ages and the influence of soil chemistry. *Meteoritics & Planetary Sciences*, *40*(8), 1215–1239. https://doi.org/10.1111/j.1945-5100.2005.tb00185.x

Anim, G. A., & Ruzicka, A. M. (2024). Electron Backscatter Diffraction (EBSD) of Shergottites Northwest Africa (NWA) 15628, NWA 12241, and Dhofar (Dho) 019. In *55th Lunar and Planetary Science Conference* (p. 1810). No. 3040.

Artemieva, N., & Ivanov, B. (2004). Launch of Martian meteorites in oblique impacts. *Icarus*, *171*(1), 84–101. https://doi.org/10.1016/j.icarus.2004.05.003

Avanzinelli, R., Boari, E., Conticelli, S., Francalanci, L., Guarnieri, L., Perini, G., et al. (2005). High precision Sr, Nd, and Pb isotopic analyses using the new generation thermal ionisation Mass Spectrometer ThermoFinnigan Triton-Ti®. *Periodico di Mineralogia*, *74*(3), 147–166. Retrieved from https://hdl.handle.net/2158/308996

Barrat, J. A., Gillet, P., Sautter, V., Jambon, A., Javoy, M., Göpel, et al. (2002). Petrology and chemistry of the basaltic shergottite North West Africa 480. *Meteoritics & Planetary Sciences*, *37*(4), 487–499. https://doi.org/10.1111/j.1945-5100.2002.tb00835.x

Benaroya, S. (2023). Olivine-orthopyroxene-spinel geothermo-oxybarometer (version 2). *Zenodo*. https://doi.org/10.5281/zenodo.7884330

Benaroya, S., Gross, J., Burger, P., Righter, M., & Lapen, T. J. (2022). Olivine-gabbroic shergottite Northwest Africa (NWA) 13227: A link between gabbroic and poikilitic shergottites? In *53rd Lunar and Planetary Science Conference, 2678*.

Benaroya, S., Gross, J., Burger, P., Righter, M., Lapen, T. J., & Eckley, S. (2024). Petrogenesis of a new type of intrusive shergottite: Olivine-gabbro Northwest Africa 13227. *Geochimica et Cosmochimica Acta*, *370*, 41–65. https://doi.org/10.1016/j.gca.2024.02.004

Bence, A. E., & Papike, J. J. (1972). Pyroxenes as recorders of lunar basalt petrogenesis: Chemical trends due to crystal-liquid interaction. In *Proceedings of the Lunar Science Conference* (Vol. 3, pp. 431–469).

Bence, A. E., Papike, J. J., & Lindsley, D. H. (1971). Crystallization history of clinopyroxenes in two porphyritic rocks from Oceanus Procellarum. In *Proceedings of the Lunar Science Conference* (Vol. 2, pp. 559–574).

Bezard, R., Fischer-Gödde, M., Hamelin, C., Brennecka, G. A., & Kleine, T. (2016). The effects of magmatic processes and crustal recycling on the molybdenum stable isotopic composition of Mid-Ocean Ridge Basalts. *Earth and Planetary Science Letters*, *453*, 171–181. https://doi.org/10.1016/j.epsl.2016.07.056

Bibring, J.-P., Hamm, V., Pilorget, C., Vago, J. L., & the MicrOmega Team (2017). The MicrOmega investigation onboard ExoMars. *Astrobiology*, *17*(6–7), 621–626. https://doi.org/10.1089/ast.2016.1642

Blichert-Toft, J., Gleason, J. D., Télouk, P., & Albarède, F. (1999). The Lu-Hf isotope geochemistry of shergottites and the evolution of the Martian mantle-crust system. *Earth and Planetary Science Letters*, *173*(1–2), 25–39. https://doi.org/10.1016/S0012-821X(99)00222-8

Bogard, D. D., Hörz, F., & Johnson, P. H. (1986). Shock-implanted noble gases: An experimental study with implications for the origin of Martian gases in shergottite meteorites. *Journal of Geophysical Research*, *91*(B13), E99–E114. https://doi.org/10.1029/JB091iB13p00E99

Bogard, D. D., & Johnson, P. (1983). Martian gases in an Antarctic meteorite? *Science*, *221*(4611), 651–654. https://doi.org/10.1126/science.221.4611.651

Bogard, D. D., Nyquist, L. E., & Johnson, P. (1984). Noble gas contents of shergottites and implications for the Martian origin of SNC meteorites. *Geochimica et Cosmochimica Acta*, *48*(9), 1723–1739. https://doi.org/10.1016/0016-7037(84)90028-0

Borg, L., & Drake, M. J. (2005). A review of meteorite evidence for the timing of magmatism and of surface or near-surface liquid water on Mars. *Journal of Geophysical Research*, *110*(E12), E12S03. https://doi.org/10.1029/2005JE002402

Borg, L. E., Brennecka, G. A., & Symes, S. J. (2016). Accretion timescale and impact history of Mars deduced from the isotopic systematics of Martian meteorites. *Geochimica et Cosmochimica Acta*, *175*, 150–167. https://doi.org/10.1016/j.gca.2015.12.002

Borg, L. E., & Draper, D. S. (2003). A petrogenetic model for the origin and compositional variation of the Martian basaltic meteorites. *Meteoritics & Planetary Sciences*, *38*(12), 1713–1731. https://doi.org/10.1111/j.1945-5100.2003.tb00011.x

Borg, L. E., Nyquist, L. E., Taylor, L. A., Wiesmann, H., & Shih, C. Y. (1997). Constraints on Martian differentiation processes from Rb-Sr and Sm-Nd isotopic analyses of the basaltic shergottite QUE94201. *Geochimica et Cosmochimica Acta*, *61*(22), 4915–4931. https://doi.org/10.1016/S0016-7037(97)00276-7

Borg, L. E., Nyquist, L. E., Wiesmann, H., & Reese, Y. (2002). Constraints on the petrogenesis of Martian meteorites from the Rb-Sr and Sm-Nd isotopic systematics of the lherzolitic shergottites ALH 77005 and LEW 88516. *Geochimica et Cosmochimica Acta*, *66*(11), 2037–2053. https://doi.org/10.1016/S0016-7037(02)00835-9

Borg, L. E., Nyquist, L. E., Wiesmann, H., Shih, C. Y., & Reese, Y. (2003). The age of Dar al Gani 476 and the differentiation history of the Martian meteorites inferred from their radiogenic isotopic systematics. *Geochimica et Cosmochimica Acta*, *67*(18), 3519–3536. https://doi.org/10.1016/S0016-7037(03)00094-2

Boulanger, M., France, L., Ferrando, C., Ildefonse, B., Ghosh, B., Sanfilippo, A., et al. (2021). Magma-mush interactions in the lower oceanic crust: Insights from Atlantis bank layered series (Southwest Indian Ridge). *Journal of Geophysical Research: Solid Earth*, *126*(9), e2021JB022331. https://doi.org/10.1029/2021JB022331

Boyd, F. R., & Smith, D. (1971). Compositional zoning in pyroxenes from lunar rock 12021, Oceanus Procellarum. *Journal of Petrology*, *12*(3), 439–464. https://doi.org/10.1093/petrology/12.3.439

Brandon, A. D., Walker, R. J., Morgan, J. W., & Goles, G. G. (2000). Re-Os isotopic evidence for early differentiation of the Martian mantle. *Geochimica et Cosmochimica Acta*, *64*(23), 4083–4095. https://doi.org/10.1016/S0016-7037(00)00482-8

Brearley, A. (1991). Subsolidus microstructures and cooling history of pyroxenes in the Zagami shergottite. In *22nd Lunar and Planetary Science Conference* (Vol. 22, p. 135).

Burbine, T. H., Buchanan, P. C., Klima, R. L., & Binzel, R. P. (2018). Can formulas derived from pyroxenes and/or HEDs be used to determine the mineralogies of V-type asteroids? *Journal of Geophysical Research: Planets*, *123*(7), 1791–1803. https://doi.org/10.1029/2018JE005561

Carli, C., Ciarniello, M., Migliorini, A., & Pratesi, G. (2022). Iron rich basaltic eucrites, implication on spectral properties and parental bodies. *Icarus*, *371*, 114653. https://doi.org/10.1016/j.icarus.2021.114653

Carli, C., Pratesi, G., Moggi-Cecchi, V., Zambon, F., Capaccioni, F., & Santoro, S. (2018). Northwest Africa 6232: Visible-near infrared reflectance spectra variability of an olivine diogenite. *Meteoritics & Planetary Sciences*, *53*(10), 2228–2242. https://doi.org/10.1111/maps.13056

Castle, N., & Herd, C. D. K. (2017). Experimental petrology of the Tissint meteorite: Redox estimates, crystallization curves, and evaluation of petrogenetic models. *Meteoritics & Planetary Sciences*, *52*(1), 125–146. https://doi.org/10.1111/maps.12739

Clark, R. N., & Roush, T. L. (1984). Reflectance spectroscopy: Quantitative analysis techniques for remote sensing applications. *Journal of Geophysical Research*, *89*(B7), 6329–6340. https://doi.org/10.1029/JB089iB07p06329

Cloutis, E. A., Gaffey, M. J., Jackowski, T. L., & Reed, K. L. (1986). Calibrations of phase abundance, composition, and particle size distribution for olivine-orthopyroxene mixtures from reflectance spectra. *Journal of Geophysical Research*, *91*(B11), 11641–11653. https://doi.org/10.1029/JB091iB11p11641

Combs, L. M., Udry, A., Howarth, G. H., Righter, M., Lapen, T. J., Gross, J., et al. (2019). Petrology of the enriched poikilitic shergottite Northwest Africa 10169: Insight into the Martian interior. *Geochimica et Cosmochimica Acta*, *266*, 435–462. https://doi.org/10.1016/j.gca.2019.07.001

Cousin, A., Sautter, V., Payré, V., Forni, O., Mangold, N., Gasnault, O., et al. (2017). Classification of igneous rocks analyzed by ChemCam at Gale crater, Mars. *Icarus*, *288*, 265–283. https://doi.org/10.1016/j.icarus.2017.01.014

Daly, L., Piazolo, S., Lee, M. R., Griffin, S., Chung, P., Campanale, F., et al. (2019). Understanding the emplacement of Martian volcanic rocks using petrofabrics of the nakhlite meteorites. *Earth and Planetary Science Letters*, *520*, 220–230. https://doi.org/10.1016/j.epsl.2019.05.050

Day, J. M. D., Paquet, M., Udry, A., & Moynier, F. (2024). A heterogeneous mantle and crustal structure formed during the early differentiation of Mars. *Science Advances*, *10*(22), eadn9830. https://doi.org/10.1126/sciadv.adn9830

Day, J. M. D., Tait, K. T., Udry, A., Moynier, F., Liu, Y., & Neal, C. R. (2018). Martian magmatism from plume metasomatized mantle. *Nature Communications*, *9*(1), 4799. https://doi.org/10.1038/s41467-018-07191-0

Debaille, V., Brandon, A. D., Yin, Q. Z., & Jacobsen, B. (2007). Coupled ^{142}Nd–^{143}Nd evidence for a protracted magma ocean in Mars. *Nature*, *450*(7169), 525–528. https://doi.org/10.1038/nature06317

Deng, Z., Moynier, F., Villeneuve, J., Jensen, N. K., Liu, D., Cartigny, P., et al. (2020). Early oxidation of the Martian crust triggered by impacts. *Science Advances*, *6*(44), eabc4941. https://doi.org/10.1126/sciadv.abc4941

Dowty, E., Keil, K., & Prinz, M. (1974). Lunar pyroxene-phyric basalts: Crystallization under supercooled conditions. *Journal of Petrology*, *15*(3), 419–453. https://doi.org/10.1093/petrology/15.3.419

Dyar, M. D. (2003). Ferric iron in SNC meteorites as determined by Mössbauer spectroscopy: Implications for Martian landers and Martian oxygen fugacity. *Meteoritics & Planetary Sciences*, *38*(12), 1733–1752. https://doi.org/10.1111/j.1945-5100.2003.tb00012.x

El Goresy, A. H. M. E. D., Ramdohr, P., & Taylor, L. A. (1971). The opaque minerals in the lunar rocks from Oceanus Procellarum. *Proceedings of the Lunar Science Conference*, *1*, 219–235.

Filiberto, J., & Dasgupta, R. (2011). Fe^{2+}–Mg partitioning between olivine and basaltic melts: Applications to genesis of olivine-phyric shergottites and conditions of melting in the Martian interior. *Earth and Planetary Science Letters*, *304*(3–4), 527–537. https://doi.org/10.1016/j.epsl.2011.02.029

Filiberto, J., Gross, J., Trela, J., & Ferré, E. C. (2014). Gabbroic shergottite northwest Africa 6963: An intrusive sample of Mars. *American Mineralogist*, *99*(4), 601–606. https://doi.org/10.2138/am.2014.4638

Filiberto, J., Gross, J., Udry, A., Trela, J., Wittmann, A., Cannon, K. M., et al. (2018). Shergottite northwest Africa 6963: A pyroxene-cumulate Martian gabbro. *Journal of Geophysical Research: Planets*, *123*(7), 1823–1841. https://doi.org/10.1029/2018JE005635

Fodor, R. V., & Moore, R. B. (1994). Petrology of gabbroic xenoliths in 1960 Kilauea basalt: Crystalline remnants of prior (1955) magmatism. *Bulletin of Volcanology*, *56*(1), 62–74. https://doi.org/10.1007/BF00279729

Franza, A., Shehaj, X., & Pratesi, G. (2024). A fistful of Mars exploring the role of Martian meteorites in cultural Heritage and scientific inquiry. *Heritage*, *7*(12), 6981–6997. https://doi.org/10.3390/heritage7120323

Friedrich, J. M., Ruzicka, A., Macke, R. J., Thostenson, J. O., Rudolph, R. A., Rivers, M. L., & Ebel, D. S. (2017). Relationships among physical properties as indicators of high temperature deformation or post-shock thermal annealing in ordinary chondrites. *Geochimica et Cosmochimica Acta*, *203*, 157–174. https://doi.org/10.1016/j.gca.2016.12.039

Fritz, J., Artemieva, N., & Greshake, A. (2005). Ejection of Martian meteorites. *Meteoritics & Planetary Sciences*, *40*(9–10), 1393–1411. https://doi.org/10.1111/j.1945-5100.2005.tb00409.x

Gaffey, M. J., Bell, J. F., Brown, R. H., Burbine, T. H., Piatek, J. L., Reed, K. L., & Chaky, D. A. (1993). Mineralogical variations within the S-type asteroid class. *Icarus*, *106*(2), 573–602. https://doi.org/10.1006/icar.1993.1194

Ghiorso, M. S., & Evans, B. W. (2008). Thermodynamics of rhombohedral oxide solid solutions and a revision of the Fe-Ti two-oxide geothermometer and oxygen-barometer. *American Journal of Science*, *308*(9), 957–1039. https://doi.org/10.2475/09.2008.01

Gross, J., Filiberto, J., Herd, C. D., Daswani, M. M., Schwenzer, S. P., & Treiman, A. H. (2013). Petrography, mineral chemistry, and crystallization history of olivine-phyric shergottite NWA 6234: A new melt composition. *Meteoritics & Planetary Sciences*, *48*(5), 854–871. https://doi.org/10.1111/maps.12092

Gross, J., Hilton, A., Prissel, T. C., Setera, J. B., Korotev, R. L., & Calzada-Diaz, A. (2020). Geochemistry and petrogenesis of Northwest Africa 10401: A new type of the Mg-suite rocks. *Journal of Geophysical Research: Planets*, *125*(5), e2019JE006225. https://doi.org/10.1029/2019JE006225

Grove, T. L., & Bence, A. E. (1977). Experimental study of pyroxene-liquid interaction in quartz-normative basalt 15597. In *8th Lunar Science Conference* (Vol. 8, pp. 1549–1579).

Grove, T. L., & Raudsepp, M. (1978). Effects of kinetics on the crystallization of quartz normative basalt 15597: An experimental study. In *9th Lunar and Planetary Science Conference* (Vol. 9, pp. 585–599).

Haloda, J., Týcová, P., Korotev, R. L., Fernandes, V. A., Burgess, R., Thöni, M., et al. (2009). Petrology, geochemistry, and age of low-Ti mare-basalt meteorite Northeast Africa 003-A: A possible member of the Apollo 15 mare basaltic suite. *Geochimica et Cosmochimica Acta*, *73*(11), 3450–3470. https://doi.org/10.1016/j.gca.2009.03.003

Harper, C. L., Jr., Nyquist, L. E., Bansal, B., Wiesmann, H., & Shih, C. Y. (1995). Rapid accretion and early differentiation of Mars indicated by ^{142}Nd/^{144}Nd in SNC meteorites. *Science*, *267*(5195), 213–217. https://doi.org/10.1126/science.7809625

Herd, C. D. K. (2003). The oxygen fugacity of olivine-phyric Martian basalts and the components within the mantle and crust of Mars. *Meteoritics & Planetary Sciences*, *38*(12), 1793–1805. https://doi.org/10.1111/j.1945-5100.2003.tb00015.x

Herd, C. D. K., Borg, L. E., Jones, J. H., & Papike, J. J. (2002). Oxygen fugacity and geochemical variations in the Martian basalts: Implications for Martian basalt petrogenesis and the oxidation state of the upper mantle of Mars. *Geochimica et Cosmochimica Acta*, *66*(11), 2025–2036. https://doi.org/10.1016/S0016-7037(02)00828-1

Herd, C. D. K., Bosak, T., Hausrath, E. M., Hickman-Lewis, K., Mayhew, L. E., Shuster, D. L., et al. (2025). Sampling Mars: Geologic context and preliminary characterization of samples collected by the NASA Mars 2020 Perseverance Rover Mission. *Proceedings of the National Academy of Sciences of the United States of America*, *122*(2), e2404255121. https://doi.org/10.1073/pnas.2404255121

Herd, C. D. K., Hamilton, J. S., Walton, E. L., Tornabene, L. L., Lagain, A., Benedix, G. K., et al. (2024). The source craters of the Martian meteorites: Implications for the igneous evolution of Mars. *Science Advances*, *10*(33), eadn2378. https://doi.org/10.1126/sciadv.adn2378

Herd, C. D. K., Walton, E. L., Agee, C. B., Muttik, N., Ziegler, Shearer, K., et al. (2017). The Northwest Africa 8159 Martian meteorite: Expanding the Martian sample suite to the early Amazonian. *Geochimica et Cosmochimica Acta*, *218*, 1–26. https://doi.org/10.1016/j.gca.2017.08.037

Hollister, L. S., Trzcienski, W. E., Jr., Hargraves, R. B., & Kulick, C. G. (1971). Petrogenetic significance of pyroxenes in two Apollo 12 samples. *Proceedings of the Lunar Science Conference*, *1*, 529–557.

Howarth, G. H., & Udry, A. (2017). Trace elements in olivine and the petrogenesis of the intermediate, olivine-phyric shergottite NWA 10170. *Meteoritics & Planetary Sciences*, *52*(2), 391–409. https://doi.org/10.1111/maps.12799

Howarth, G. H., Udry, A., & Day, J. M. D. (2018). Petrogenesis of basaltic shergottite Northwest Africa 8657: Implications for fO_2 correlations and element redistribution during shock melting in shergottites. *Meteoritics & Planetary Sciences*, *53*(2), 249–267. https://doi.org/10.1111/maps.12999

Hu, J., Asimow, P. D., Liu, Y., & Ma, C. (2023). Shock-recovered maskelynite indicates low-pressure ejection of shergottites from Mars. *Science Advances*, *9*(18), eadf2906. https://doi.org/10.1126/sciadv.adf2906

Hui, H., Peslier, A. H., Lapen, T. J., Shafer, J. T., Brandon, A. D., & Irving, A. J. (2011). Petrogenesis of basaltic shergottite Northwest Africa 5298: Closed-system crystallization of an oxidized mafic melt. *Meteoritics & Planetary Sciences*, *46*(9), 1313–1328. https://doi.org/10.1111/j.1945-5100.2011.01231.x

Humayun, M., Nemchin, A., Zanda, B., Hewins, R. H., Grange, M., Kennedy, A., et al. (2013). Origin and age of the earliest Martian crust from meteorite NWA 7533. *Nature*, *503*(7477), 513–516. https://doi.org/10.1038/nature12764

Irving, A. J., Kuehner, S. M., Carpenter, P. K., Moser, D. E., Barker, I., Righter, M., et al. (2018). Petrologic, isotopic, and elemental characterization of shock-melted intermediate olivine gabbroic shergottite Northwest Africa 11509. In *49th Annual Lunar and Planetary Science Conference. No. 2083* (p. 2279).

Irving, A. J., Kuehner, S. M., Herd, C., Gellissen, M., Korotev, R. L., Puchtel, I., et al. (2010). Petrologic, elemental and multi-isotopic characterization of permafic olivine-phyric shergottite Northwest Africa 5789: A primitive magma derived from depleted Martian mantle. In *41th Lunar and Planetary Science Conference, 1547*.

Jamsja, N., & Ruzicka, A. (2010). Shock and thermal history of Northwest Africa 4859, an annealed impact-melt breccia of LL chondrite parentage containing unusual igneous features and pentlandite. *Meteoritics & Planetary Sciences*, *45*(5), 828–849. https://doi.org/10.1111/j.1945-5100.2010.01056.x

Kizovski, T. V., Tait, K. T., Di Cecco, V. E., White, L. F., & Moser, D. E. (2019). Detailed mineralogy and petrology of highly shocked poikilitic shergottite Northwest Africa 6342. *Meteoritics & Planetary Sciences*, *54*(4), 768–784. https://doi.org/10.1111/maps.13255

Klima, R. L., Dyar, M. D., & Pieters, C. M. (2011). Near-infrared spectra of clinopyroxenes: Effects of calcium content and crystal structure. *Meteoritics & Planetary Sciences*, *46*(3), 379–395. https://doi.org/10.1111/j.1945-5100.2010.01158.x

Klima, R. L., Pieters, C. M., & Dyar, M. D. (2007). Spectroscopy of synthetic mg-fMg-Fe pyroxenes I: Spin-allowed and spin-forbidden crystal field bands in the visible and near-infrared. *Meteoritics & Planetary Sciences*, *42*(2), 235–253. https://doi.org/10.1111/j.1945-5100.2007.tb00230.x

Klima, R. L., Pieters, C. M., & Dyar, M. D. (2008). Characterization of the 1.2 μm M1 pyroxene band: Extracting cooling history from near-IR spectra of pyroxenes and pyroxene-dominated rocks. *Meteoritics & Planetary Sciences*, *43*(10), 1591–1604. https://doi.org/10.1111/j.1945-5100.2008.tb00631.x

Kurihara, T., Mikouchi, T., Saruwatari, K., Kameda, J., & Miyamoto, M. (2008). Transmission electron microscopy of olivine in the LAR 06319 olivine-phyric shergottite. *Meteoritics and Planetary Science Supplement*, *43*, 5177.

Lapen, T. J., Righter, M., Brandon, A. D., Debaille, V., Beard, B. L., Shafer, J. T., & Peslier, A. H. (2010). A younger age for ALH84001 and its geochemical link to shergottite sources in Mars. *Science*, *328*(5976), 347–351. https://doi.org/10.1126/science.1185395

Le Maitre, R. W., Streckeisen, A., Zanettin, B., Le Bas, M. J., Bonin, B., Bateman, P., et al. (2002). *Igneous rocks: A classification and glossary of terms: Recommendations of the International Union of Geological Sciences subcommission on the systematics of igneous rocks* (2nd ed.). Cambridge University Press.

Liu, Y., Baziotis, I. P., Asimow, P. D., Bodnar, R. J., & Taylor, L. A. (2016). Mineral chemistry of the Tissint meteorite: Indications of two-stage crystallization in a closed system. *Meteoritics & Planetary Sciences*, *51*(12), 2293–2315. https://doi.org/10.1111/maps.12726

Liu, Y., Tice, M. M., Schmidt, M. E., Treiman, A. H., Kizovski, T. V., Hurowitz, J. A., et al. (2022). An olivine cumulate outcrop on the floor of Jezero crater, Mars. *Science*, *377*(6614), 1513–1519. https://doi.org/10.1126/science.abo2756

Lodders, K. (2003). Solar system abundances and condensation temperatures of the elements. *The Astrophysical Journal*, *591*(2), 1220–1247. https://doi.org/10.1086/375492

Longhi, J., & Pan, V. (1989). The parent magmas of the SNC meteorites. In *Proceeding of the 19th Lunar and Planetary Science Conference* (pp. 451–464).

Malarewicz, V., Beyssac, O., Zanda, B., Marin-Carbonne, J., Leroux, H., Rubatto, D., et al. (2025). Evidence for pre-Noachian granitic rocks on Mars from quartz in meteorite NWA 7533. *Nature Geoscience*, *18*(3), 207–212. https://doi.org/10.1038/s41561-025-01653-z

Mandon, L., Beck, P., Quantin-Nataf, C., Dehouck, E., Pommerol, A., Yoldi, Z., et al. (2021). Martian meteorites reflectance and implications for rover missions. *Icarus*, *366*, 114517. https://doi.org/10.1016/j.icarus.2021.114517

Mandon, L., Quantin-Nataf, C., Royer, C., Beck, P., Fouchet, T., Johnson, J. R., et al. (2023). Reflectance of Jezero crater floor: 2. Mineralogical interpretation. *Journal of Geophysical Research: Planets*, *128*(7), e2022JE007450. https://doi.org/10.1029/2022JE007450

Mangold, N., Schmidt, M. E., Fisk, M. R., Forni, O., McLennan, S. M., Ming, D. W., et al. (2017). Classification scheme for sedimentary and igneous rocks in Gale crater, Mars. *Icarus*, *284*, 1–17. https://doi.org/10.1016/j.icarus.2016.11.005

McCubbin, F. M., Farley, K. A., Harrington, A. D., Hutzler, A., & Smith, C. L. (2025). Mars sample return: From collection to curation of samples from a habitable world. *Proceedings of the National Academy of Sciences of the United States of America*, *122*(2), e2404253121. https://doi.org/10.1073/pnas.2404253121

McDonough, W. F., & Sun, S. S. (1995). The composition of the Earth. *Chemical Geology*, *120*(3–4), 223–253. https://doi.org/10.1016/0009-2541(94)00140-4

McFarlane, C. R., & Spray, J. G. (2022). The Los Angeles Martian diabase: Phosphate U-Th-Pb geochronology and mantle source constraints. *Geochimica et Cosmochimica Acta*, *326*, 166–179. https://doi.org/10.1016/j.gca.2022.04.006

McSween, H. Y., Jr. (1984). SNC meteorites: Are they Martian rocks? *Geology*, *12*(1), 3–6. https://doi.org/10.1130/0091-7613(1984)12<3:smatmr>2.0.co;2

McSween, H. Y., Jr. (1994). What we have learned about Mars from SNC meteorites. *Meteoritics*, *29*(6), 757–779. https://doi.org/10.1111/j.1945-5100.1994.tb01092.x

McSween, H. Y., Jr. (2015). Petrology on mars. *American Mineralogist*, *100*(11–12), 2380–2395. https://doi.org/10.2138/am-2015-5257

Mcsween, H. Y., Jr., Eisenhour, D. D., Taylor, L. A., Wadhwa, M., & Crozaz, G. (1996). QUE94201 shergottite: Crystallization of a Martian basaltic magma. *Geochimica et Cosmochimica Acta*, *60*(22), 4563–4569. https://doi.org/10.1016/S0016-7037(96)00265-7

McSween, H. Y., Jr., & Stöffler, D. (1980). Shock metamorphic features in Allan Hills 77005 meteorite. *Lunar and Planetary Science*, *11*, 717–719.

McSween, H. Y., Jr., Taylor, G. J., & Wyatt, M. B. (2009). Elemental composition of the Martian crust. *Science*, *324*(5928), 736–739. https://doi.org/10.1126/science.1165871

Meteoritical Bulletin Database. (2025). Retrieved from https://www.lpi.usra.edu/meteor/

Mikouchi, T., Miyamoto, M., & McKay, G. A. (1998). Mineralogy of Antarctic basaltic shergottite Queen Alexandra Range 94201: Similarities to Elephant Moraine A79001 (lithology B) Martian meteorite. *Meteoritics & Planetary Sciences*, *33*(2), 181–189. https://doi.org/10.1111/j.1945-5100.1998.tb01624.x

Mikouchi, T., Miyamoto, M., & McKay, G. A. (1999). The role of undercooling in producing igneous zoning trends in pyroxenes and maskelynites among basaltic Martian meteorites. *Earth and Planetary Science Letters*, *173*(3), 235–256. https://doi.org/10.1016/S0012-821X(99)00188-0

Mittlefehldt, D. W. (1994). ALH84001, a cumulate orthopyroxenite member of the Martian meteorite clan. *Meteoritics*, *29*(2), 214–221. https://doi.org/10.1111/j.1945-5100.1994.tb00673.x

Nicklas, R. W., Day, J. M. D., Vaci, Z., Udry, A., Liu, Y., & Tait, K. T. (2021). Uniform oxygen fugacity of shergottite mantle sources and an oxidized Martian lithosphere. *Earth and Planetary Science Letters*, *564*, 116876. https://doi.org/10.1016/j.epsl.2021.116876

Nyquist, L. E., Bogard, D. D., Shih, C. Y., Park, J., Reese, Y. D., & Irving, A. J. (2009). Concordant Rb–Sr, Sm–Nd, and Ar–Ar ages for Northwest Africa 1460: A 346 Ma old basaltic shergottite related to "lherzolitic" shergottites. *Geochimica et Cosmochimica Acta*, *73*(14), 4288–4309. https://doi.org/10.1016/j.gca.2009.04.008

Ostertag, R., Amthauer, G., Rager, H., & McSween Jr, H. Y. (1984). Fe^{3+} in shocked olivine crystals of the ALHA 77005 meteorite. *Earth and Planetary Science Letters*, *67*(2), 162–166. https://doi.org/10.1016/0012-821X(84)90111-0

Papike, J. J., Karner, J. M., Shearer, C. K., & Burger, P. V. (2009). Silicate mineralogy of Martian meteorites. *Geochimica et Cosmochimica Acta*, *73*(24), 7443–7485. https://doi.org/10.1016/j.gca.2009.09.008

Peslier, A. H., Hnatyshin, D., Herd, C. D. K., Walton, E. L., Brandon, A. D., Lapen, T. J., & Shafer, J. T. (2010). Crystallization, melt inclusion, and redox history of a Martian meteorite: Olivine-phyric shergottite Larkman Nunatak 06319. *Geochimica et Cosmochimica Acta*, *74*(15), 4543–4576. https://doi.org/10.1016/j.gca.2010.05.002

Righter, M., Lapen, T. J., & Irving, A. J. (2019). Sm-Nd and Lu-Hf isotopic systematics of shock-melted intermediate olivine gabbroic shergottite Northwest Africa 11509. In *50th Annual Lunar and Planetary Science Conference, No. 2132* (p. 2940).

Royer, C., Poulet, F., Wiens, R. C., Montmessin, F., Beck, P., Beyssac, O., et al. (2025). The mineralogical composition of Jezero Crater Western Fan: Multigaussian modeling of Perseverance/SuperCam near-infrared observations and overview of major units. *Icarus*, *434*, 116538. https://doi.org/10.1016/j.icarus.2025.116538

Ruzicka, A. M., & Hugo, R. C. (2018). Electron backscatter diffraction (EBSD) study of seven heavily metamorphosed chondrites: Deformation systematics and variations in pre-shock temperature and post-shock annealing. *Geochimica et Cosmochimica Acta*, *234*, 115–147. https://doi.org/10.1016/j.gca.2018.05.014

Sack, R. O., & Ghiorso, M. S. (1989). Importance of considerations of mixing properties in establishing an internally consistent thermodynamic database: Thermochemistry of minerals in the system Mg_2SiO_4-Fe_2SiO_4-SiO_2. *Contributions to Mineralogy and Petrology*, *102*(1), 41–68. https://doi.org/10.1007/BF01160190

Sack, R. O., & Ghiorso, M. S. (1991a). Chromian spinels as petrogenetic indicators: Thermodynamics and petrological applications. *American Mineralogist*, *76*(5–6), 827–847.

Sack, R. O., & Ghiorso, M. S. (1991b). An internally consistent model for the thermodynamic properties of Fe(Mg-titanomagnetite-aluminate spinels. *Contributions to Mineralogy and Petrology*, *106*(4), 474–505. https://doi.org/10.1007/BF00321989

Sack, R. O., & Ghiorso, M. S. (1994a). Thermodynamics of multicomponent pyroxenes: I. Formulation of a general model. *Contributions to Mineralogy and Petrology*, *116*(3), 277–286. https://doi.org/10.1007/BF00306497

Sack, R. O., & Ghiorso, M. S. (1994b). Thermodynamics of multicomponent pyroxenes: II. Phase relations in the quadrilateral. *Contributions to Mineralogy and Petrology*, *116*(3), 287–300. https://doi.org/10.1007/BF00306498

Sack, R. O., & Ghiorso, M. S. (1994c). Thermodynamics of multicomponent pyroxenes: III. Calibration of $Fe^{2+}(Mg)_{-1}$, $TiAl_2(MgSi_2)_{-1}$, $TiFe^{3+}_2(MgSi_2)_{-1}$, $AlFe^{3+}(MgSi)_{-1}$, $NaAl(CaMg)_{-1}$, $Al_2(MgSi)_{-1}$ and $Ca(Mg)_{-1}$ exchange reactions between pyroxenes and silicate melts. *Contributions to Mineralogy and Petrology*, *118*(3), 271–296. https://doi.org/10.1007/BF00306648

Saper, L., Liu, Y., Kipp, M. A., Burney, D., Ma, C., Tissot, F. L., et al. (2025). Chemical, isotopic (O, He, U), and petrological characteristics of a slowly cooled enriched gabbroic shergottite, Northwest Africa 13134. *Meteoritics & Planetary Sciences*, *60*(5), 1119–1150. https://doi.org/10.1111/maps.14345

Sarbadhikari, A. B., Day, J. M. D., Liu, Y., Rumble, D., III., & Taylor, L. A. (2009). Petrogenesis of olivine-phyric shergottite Larkman Nunatak 06319: Implications for enriched components in Martian basalts. *Geochimica et Cosmochimica Acta*, *73*(7), 2190–2214. https://doi.org/10.1016/j.gca.2009.01.012

Sautter, V., Toplis, M. J., Beck, P., Mangold, N., Wiens, R., Pinet, P., et al. (2016). Magmatic complexity on early Mars as seen through a combination of orbital, in-situ and meteorite data. *Lithos*, *254*, 36–52. https://doi.org/10.1016/j.lithos.2016.02.023

Shehaj, X. (2025). Northwest Africa (NWA) 16788: A new olivine microgabbroic shergottite. Insights into Martian magmatism from the largest individual meteorite from Mars (version 1). Dataset. *Zenodo*. https://doi.org/10.5281/zenodo.15401894

Smyth, J. R., & McCormick, T. C. (1995). Crystallographic data for minerals. *Mineral Physics and Crystallography: A Handbook of Physical Constants*, *2*, 1–17. https://doi.org/10.1029/rf002p0001

Stöffler, D., Hamann, C., & Metzler, K. (2018). Shock metamorphism of planetary silicate rocks and sediments: Proposal for an updated classification system. *Meteoritics & Planetary Sciences*, *53*(1), 5–49. https://doi.org/10.1111/maps.12912

Stöffler, D., Keil, K., & Scott, E. R. D. (1991). Shock metamorphism of ordinary chondrites. *Geochimica et Cosmochimica Acta*, *55*(12), 3845–3867. https://doi.org/10.1016/0016-7037(91)90078-J

Stöffler, D., Ostertag, R., Jammes, C., Pfannschmidt, G., Gupta, P. S., Simon, S. B., et al. (1986). Shock metamorphism and petrography of the Shergotty achondrite. *Geochimica et Cosmochimica Acta*, *50*(6), 889–903. https://doi.org/10.1016/0016-7037(86)90371-6

Stormer, J. C., Pierson, M. L., & Tacker, R. C. (1993). Variation of F and Cl X-ray intensity due to anisotropic diffusion in apatite during electron microprobe analysis. *American Mineralogist*, *78*(5–6), 641–648.

Symes, S. J., Borg, L. E., Shearer, C. K., & Irving, A. J. (2008). The age of the Martian meteorite Northwest Africa 1195 and the differentiation history of the shergottites. *Geochimica et Cosmochimica Acta*, *72*(6), 1696–1710. https://doi.org/10.1016/j.gca.2007.12.022

Thirlwall, M. F. (1991). Long-term reproducibility of multicollector Sr and Nd isotope ratio analysis. *Chemical Geology: Isotope Geoscience section*, *94*(2), 85–104. https://doi.org/10.1016/0168-9622(91)90002-E

Udry, A., Howarth, G. H., Herd, C. D. K., Day, J. M. D., Lapen, T. J., & Filiberto, J. (2020). What Martian meteorites reveal about the interior and surface of Mars. *Journal of Geophysical Research: Planets*, *125*(12), e2020JE006523 2doi. https://doi.org/10.1029/2020JE006523

Udry, A., Howarth, G. H., Lapen, T. J., & Righter, M. (2017). Petrogenesis of the NWA 7320 enriched Martian gabbroic shergottite: Insight into the Martian crust. *Geochimica et Cosmochimica Acta*, *204*, 1–18. https://doi.org/10.1016/j.gca.2017.01.032

Udry, A., Ostwald, A., Sautter, V., Cousin, A., Beyssac, O., Forni, O., et al. (2023). A Mars 2020 Perseverance SuperCam perspective on the igneous nature of the Máaz formation at Jezero crater and link with Séítah, Mars. *Journal of Geophysical Research: Planets*, *128*(7), e2022JE007440. https://doi.org/10.1029/2022JE007440

Udry, A., Ostwald, A. M., Day, J. M. D., & Hallis, L. J. (2025). Fundamental constraints and questions from the study of Martian meteorites and the need for returned samples. *Proceedings of the National Academy of Sciences of the United States of America*, *122*(2), e2404254121. https://doi.org/10.1073/pnas.2404254121

Van de Moortèle, B., Reynard, B., Rochette, P., Jackson, M., Beck, P., Gillet, P., et al. (2007). Shock-induced metallic iron nanoparticles in olivine-rich Martian meteorites. *Earth and Planetary Science Letters*, *262*(1–2), 37–49. https://doi.org/10.1016/j.epsl.2007.07.002

Wiens, R. C., & Pepin, R. O. (1988). Laboratory shock emplacement of noble gases, nitrogen, and carbon dioxide into basalt, and implications for trapped gases in shergottite EETA 79001. *Geochimica et Cosmochimica Acta*, *52*(2), 295–307. https://doi.org/10.1016/0016-7037(88)90085-3

Wlotzka, F. (1993). A weathering scale for the ordinary chondrites. *Meteoritics*, *28*, 460.

Wones, D. R., & Gilbert, M. C. (1969). The fayalite-magnetite-quartz assemblage between 600 and 800 C. *American Journal of Science*, *267*, 480–488. https://doi.org/10.2475/001c.125321

Wu, Y., Hsu, W., Liao, S., Xiao, Z., Che, X., Pan, L., et al. (2023). Petrology and mineralogy of the Martian olivine gabbroic shergottite Northwest Africa 13581: Insights into the enriched Martian mantle source. *Geochimica et Cosmochimica Acta*, *358*, 108–125. https://doi.org/10.1016/j.gca.2023.08.003

Xirouchakis, D., Draper, D. S., Schwandt, C. S., & Lanzirotti, A. (2002). Crystallization conditions of Los Angeles, a basaltic Martian meteorite. *Geochimica et Cosmochimica Acta*, *66*(10), 1867–1880. https://doi.org/10.1016/S0016-7037(01)00892-4

References From the Supporting Information

Bouvier, A., Vervoort, J. D., & Patchett, P. J. (2008). The Lu–Hf and Sm–Nd isotopic composition of CHUR: Constraints from unequilibrated chondrites and implications for the bulk composition of terrestrial planets. *Earth and Planetary Science Letters*, *273*(1–2), 48–57. https://doi.org/10.1016/j.epsl.2008.06.010